Friedrich-Alexander-Universität
Technische Fakultät

Department Chemie- und Bioingenieurwesen (CBI)
Lehrstuhl für Energieverfahrenstechnik
Prof. Dr.-Ing. Jürgen Karl
Prof. Dr. Katharina Herkendell

Bachelor Thesis

Senlu Lin

CFD Simulation of Catalytic Methanation with a Conic Shape of the Reactor Bed

Supervisor: Xu Fang, M.Sc.

Examiner: Prof. Dr.-Ing. Jürgen Karl/Prof. Dr. Katharina Herkendell

Matriculation number: 23261684

Nürnberg, 21. Juli 2023

EIDESSTATTLICHE ERKLÄRUNG

Hiermit versichere ich, die vorliegende Arbeit selbstständig und ohne Hilfe Dritter angefertigt zu haben. Gedanken und Zitate, die ich aus fremden Quellen direkt oder indirekt übernommen habe, sind als solche kenntlich gemacht. Diese Arbeit hat in gleicher oderähnlicher Form noch keiner Prüfungsbehörde vorgelegen und wurde bisher nicht veröffentlicht. Ich erkläre mich hiermit einverstanden, dass die Arbeit durch den Lehrstuhl für Energieverfahrenstechnik der Öffentlichkeit zugänglich gemacht werden kann.

Nürnberg, 21. Juli 2023 _____Senlu, Lin_____

Vorname, Nachname

ABSTRACT

Power-to-Gas is known as a promising technology, that is mainly based on methanation, to solve the current greenhouse gas related problems and treat the carbon in the atmosphere. In this context, the theory behind the mentioned technology has been explained and a general overview of its state-of-art has been given. “ADDMeth’’ is a novel methanation reactor developed by the Chair of Energy Process Engineering at FAU (Friedrich-Alexander-University Erlangen-Nurnberg) that uses additive manufacturing and shifting diameter to achieve a better efficiency of the process. In this work, with the help of computational tools, CFD-simulations of three different scenarios are presented and analyzed independently to see how it affects the resulting efficiency of the reactor. This includes: a first scenario where the heat transfer coefficient is a variable, but the geometry and reaction rate is fixed; a second scenario where the reaction rate is changed with the geometry and heat transfer being fixed; and finally, different geometries will be tested whilst maintaining heat transfer and reaction rate constant. The objectives are to achieve an extended area within the reactor of high working temperature as well as an improved temperature handling, making “ADDMeth” a double-function reactor where both methanation and tar hydrogenation happen at the same time. A comparison and a final conclusion are given with an aim to provide the current development with new possible researching paths. The results showed how changing directly the reaction rate was the most effective way to shift the heat distribution of the reactor, changing the heat transfer coefficient affects only the maximum reacting temperature, and at last, changing the geometry displaces the location where the highest concentration of reaction occurs, as well as variation to the methane yield.

INDEX

LIST OF FIGURES

LIST OF TABLES

ABBREVIATIONS

CFD	Computational Fluid Dynamics
UDM	User Defined Memory
TPR	Temperature programmed reduction
LPM	Liquid-Phase methanation
PSI	Paul Scherrer Institute
SNG	Synthetic natural gas
ECN	Energy research center of the Netherlands
EPFL	École Polytechnique Fédérale de Lausanne
AER	Absorption enhanced reforming
URF	Under-relaxation factor
LHHW	Langmuir-Hinshelwood-Hougen-Watson

SYMBOLS USED

ΔH_r	[J/mol]	Enthalpy of reaction
k_i	[differs]	Reaction rate coefficient
r	[Kg/m^3 S]	Initial reaction rate
ξ	[Kg/m^3 S]	Actual reaction rate
K_i	[-]	Adsorption constant
E_A	[J/mol]	Activation energy
ΔH_{Ads}	[J/mol · K]	Adsorption heat
R	[J/mol · K]	Universal constant of ideal gas
T	[k]	Temperature
p	[k]	Pressure
v	[m^3]	Volume
p_i	[Pa]	Partial pressure
x	[mm]	x coordinate
y	[mm]	y coordinate
z	[mm]	z coordinate
Δy	[mm]	Change of y coordinate
β	[-]	Effectiveness factor
ε	[-]	Porosity
λ_{fluid}	[W/mK]	Heat transfer coefficient of the fluid
λ_{solid}	[W/mK]	Heat transfer coefficient of the solid
$\lambda_{\text{eff,parallel}}$	[W/mK]	Effective heat transfer coefficient
Ø	[mm]	Diameter
n	[mol]	Amount of substance
Ψ	[-]	Representation of a cell in figure 11
α	[-]	Representation of URF in figure 11

1.Introduction

The energy transition, as well as carbon neutrality, are arguably the most prominent issues the humankind is facing, between the greater commonly shared challenges by humanity. Evidently, it is crucial to a sustainable development and progress of the global civilization for the nearest future. However, this is not only an ecological or moral issue, but also a geopolitical matter, in which every country is trying to find a path towards energy independence, with a view to become more self-sufficient.

In the technological aspect, renewable energy can still not satisfy the demand by the society by far. Hence, it is necessary to find another solution, that needs to be friendly to the atmosphere, whilst being technologically and economically feasible.

Most of the renewable sources are intermittent in nature, this results in big fluctuations and unsteadiness when producing energy, making them not reliable and inconsistent when demanding big amounts of energy. The reason to this, among others, is its dependency on the surrounding, such as the weather, the terrain, or any other resource constraints. For instance, solar energy production is low in a cloudy day, or it is also low if the panels are shadowed by the mountains or any other barriers nearby [1].

The explained intermittency is one of the main reasons that makes this type of energy being insufficient. In addition to this, their energy density is also low, meaning that big amount of land is needed to produce little energy in comparison to traditional energy sources. The mentioned reasons are all related to its nature, thus, either hard to solve or the solution is already mature enough that makes it difficult to progress.

It is also well known that currently, the storage of this electrical power is still not possible, due to the flaws of its technology. However, it therefore turns it into one of the most researched topics, with the aim to increase production of renewable energy. There is a surplus in the production of renewable energies. For example, the wind energy produced by the wind farm in its peak is usually not used in its integrity, and some power must be assumed lost due to the impossibility to store them. [2] Here, Power to Gas comes into play and is the technology that is promising and widely investigated to make profit of this loss.

As it is named, this technology is designated to produce gaseous fuel from electric power. It represents a way to store energy, that will produce hydrogen through electrolysis, utilizing electrical power from the above-mentioned surplus energy. This electricity will split water into oxygen and hydrogen, and then, the produced hydrogen will be used to produce methane (gas) through methanation and finally inserted into the gas grid [3].

This method enables the possibility to integrate renewable energy with existing natural gas infrastructure, i.e., it creates the possibility to store renewable electrical energy without the need to build new networks and therefore saving huge amounts of capital investment [4]. It also makes the usage of this electrical power flexible: it can perform as a battery, storing energy when the demand is low and production is high, and releasing it when vice versa, by producing electricity with the methane yield. [5]

Additionally, its contribution to carbon reduction is notorious, as this carbon will be needed to create the methane through a chemical reaction [6].

This chemical reaction is the process of methanation, where hydrogen and carbon dioxide react to produce methane and water. This is done through a methanation reactor under certain thermodynamic conditions and the presence of a catalyst. This methanation therefore becomes the key to the power to gas technology.

Nevertheless, this process has some limits. First, the reaction requires high reacting temperature to reach sufficient reaction rate. However, if it goes excessive, it will bring some other major problems, such as catalyst deactivation or hot spots, that are harmful to the reactor. Moreover, kinetic reaction is not always as desired, it can be slow requiring longer residence times, and eventually making it difficult to be profitable. All these factors are crucial to the efficiency of the reaction and thus, to the economic viability. The stated problems are the main reasons that needs to be resolved to achieve an eventual scaled-up production of the technology [7, 8].

With the view to address the above-explained problems, the Chair of Energy Process Engineering of the Friedrich-Alexander-University Erlangen-Nurnberg has developed a fixed-bed methanation reactor with the help of additive manufacturing technology, which intends to maximize the effectiveness of Power-to-Gas reaction, as well as to reduce the investment cost. The reactor is investigated under an innovative project called “ADDmeth” and it intends to take the maximum advantage of this relatively novel manufacturing method. It grants more freedoms since the very beginning, by being less restrictive in the design stage and thus, lowering kinetic and thermodynamic limitations. It also makes use of a lattice structure to preheat feed gas and gaining some mechanical stabilization. Furthermore, the control of temperature will be better to avoid the so-called “hot spots”, this is achieved by implementing a conical reaction channel, which expands from ⌀ 8mm to 32mm. Additionally, to increase and keep the conversion rate at the highest possible, it uses only one reactor stage, simplifying the process as much as possible. Finally, to avoid loss of methane yield due to kinetic limitations, longer local residence time are considered at the reactor outlet, and increased reaction temperatures are contemplated, resulting in an improved reaction control [9].

In reality, “ADDmeth” is an uncompleted project that still undergoes researching for a continuous improvement [10]. This paper will propose geometrical changes of the reactor as a solution and discuss about the shifts to its effectiveness. This is done to have a better control of the temperature scheme and a more even distribution, which should lead to a higher efficiency of the reactor, meanwhile avoiding hot spots and deactivation of the catalyst. Additionally, this situation can also be enhanced massively by finding a suitable heat transfer coefficient of the catalyst, an appropriate pore diffusion and modifying the reaction rate, along with choosing a suitable kinetic model. Various models are already being used, but the best ones are still yet to be discovered.

The explained method will be also helpful in decomposition of tar, this will be achieved through hydrogenation, where tar will be converted into new clean fuels [11]. To summarize, the goal is to obtain a “new” ADDmeth with the characteristics and capability where both methanation and hydrogenation can be executed

simultaneously, finding the optimum geometry and thermodynamic parameters that gives the maximum effectiveness possible of the methanation reactor, and therefore maximizing the resulting methane yield, along with profitable hydrogenation of tars.

In light of the explained theories, three researching scenarios will be given in this paper: changes to heat transfer coefficient whilst unvarying geometry and pore diffusion effect (first scenario); changes to the pore diffusion effect (reaction rate) whilst maintaining geometry and heat transfer constant (second scenario); and finally geometrical shifts whilst maintaining both pore diffusion and heat transfer constant (third scenario).

Finally, to accomplish such proposed objective, CFD-simulations of the reaction will be implemented, hence some computational tools will become needed: Catia V5, Ansys ICEM, and Ansys Fluent. An explanation of each program will be given, and the paper they play in the research will be explained. These simulations will help to prevent and reduce the safety and financial risks, while applying newly discovered geometries and parameters.

2.FUNDAMENTALS

2.1 METHANATION

Methanation is the process of obtaining methane (CH_4) and water (H_2O), by reacting hydrogen (H_2) and carbon dioxide (CO_2). It is a promising approach to address the CO_2 problem and it is typically carried out under the presence of a catalyst, as otherwise the reaction would be extremely slow, moreover, it is a highly exothermic process, resulting in elevated reacting temperatures and pressures. Its lofty power density and its possibility to use waste heat makes it one of the best suited options for medium and large scale methanation plants [12]. The resulting methane can be stored, transported and used as fuel with high energy density and combustion efficiency.

The three main catalytic methods for CO_2 methanation that are being investigated widely are photocatalysis, electrocatalysis and thermal catalysis. The last one is the most efficient and compatible with the industry although being selective and operated under high temperatures. The other two methods are more environmentally friendly, but their methane yield performance is poor [47,48,49]. The activity and stability of CO_2 methanation depends primarily on the activation of H_2 and CO_2 (reactants) and the removal of coke. Their concentration (active sites) can be increased by modifying preparation methods, and sintering can be avoided by inhibiting metal particle growth. On the other hand, surface basicity and oxygen defects affect CO_2 adsorption and bond-breaking, this oxidation reaction also promotes carbon elimination. An inter-relationship between these modifications to the catalysts exists and can potentially be research areas to improve CO_2 methanation [46], however they are beyond the objective of this work.

The most typically used catalysts are those based on transition metals, with Nickel (Ni), Cobalt (Co), and Ruthenium (Ru) as the preferred ones. Ruthenium is the most stable and active but associates to a high cost. Nickel is also active but tends to deactivate, although it is the most popular option for the industries due to its low price and wide availability, in addition to this, its activity is similar to cobalt. These materials are often reinforced by support material such as alumina (Al2O3), that increases the reacting surface area and hence reduces porosity, they play a crucial role in achieving high selectivity and activity [13]. The catalysts must also be active enough at low temperatures but showing great resistance against sintering and deactivation phenomena at high temperature [14]. Promoters are sometimes used to improve even more the performance of supported catalyst, for instance, MgO can increase carbon resistance and thermal stability of Ni/Al_2O_3, CeO_2 can improve reducibility and long-term stability [13,57]. Nickel-based methanation catalysts typically undergoes a reduction (increased temperature and hydrogen atmosphere) process before applied, which occurs in a hydrogen atmosphere between 300 to 600^{o}C. This is done to obtain behavioral information by TPR (temperature programmed reduction) that may eventually provide with important information on optimum activation conditions. Finally, catalyst deactivation can occur generally as a result of chemical, thermal or mechanical reasons. Chemical deactivation includes catalyst poisoning by gas impurities and Vapor-solid reactions in a minor grade. Thermal deactivation includes

thermal degradation that induces a loss of active surface area, it is the major problem in fixed-bed reactors. And ultimately, mechanical deactivation includes fouling, that is physical deposition of species from fluid phase onto the catalytic surface and into catalyst pores, as well as attrition and crushing, which is a principal problem when it comes to fluidized-bed reactors [13,58,59] . ADDmeth uses “nial50” as catalyst, with a better selectivity, activity and stability, that is developed thoroughly by the department. CO_2 can be obtained directly via carbon capture or biogas production, and H_2 can be collected from electrolysis or gasification.

The equations of methanation are all reversible, forward and reverse reactions happen at the same time. Also, according to Le Chatelier’s principle, if higher pressures and lower temperatures are employed, the equilibrium position will be shifted towards methane, causing a higher methane yield. Under such low temperatures, CO_2 can be nearly converted into CH_4 completely [15]. This is shown in figure 1, where the simulation performed by Gao et al. shows how CO_2 conversion, and therefore CH4 yield increases with pressure but also decreases with temperature (Fig.1a, Fig.1c) at temperatures below 600ºC. Furthermore, CH_4 selectivity has a similar behavior to them according to figure 1b. In addition to this, the simulation did not generate any carbon, it was suppressed by water during the CO_2 methanation [16], as carbon deposition should not occur when H_2/CO_2 ratio is equal or greater than the stoichiometric [15].

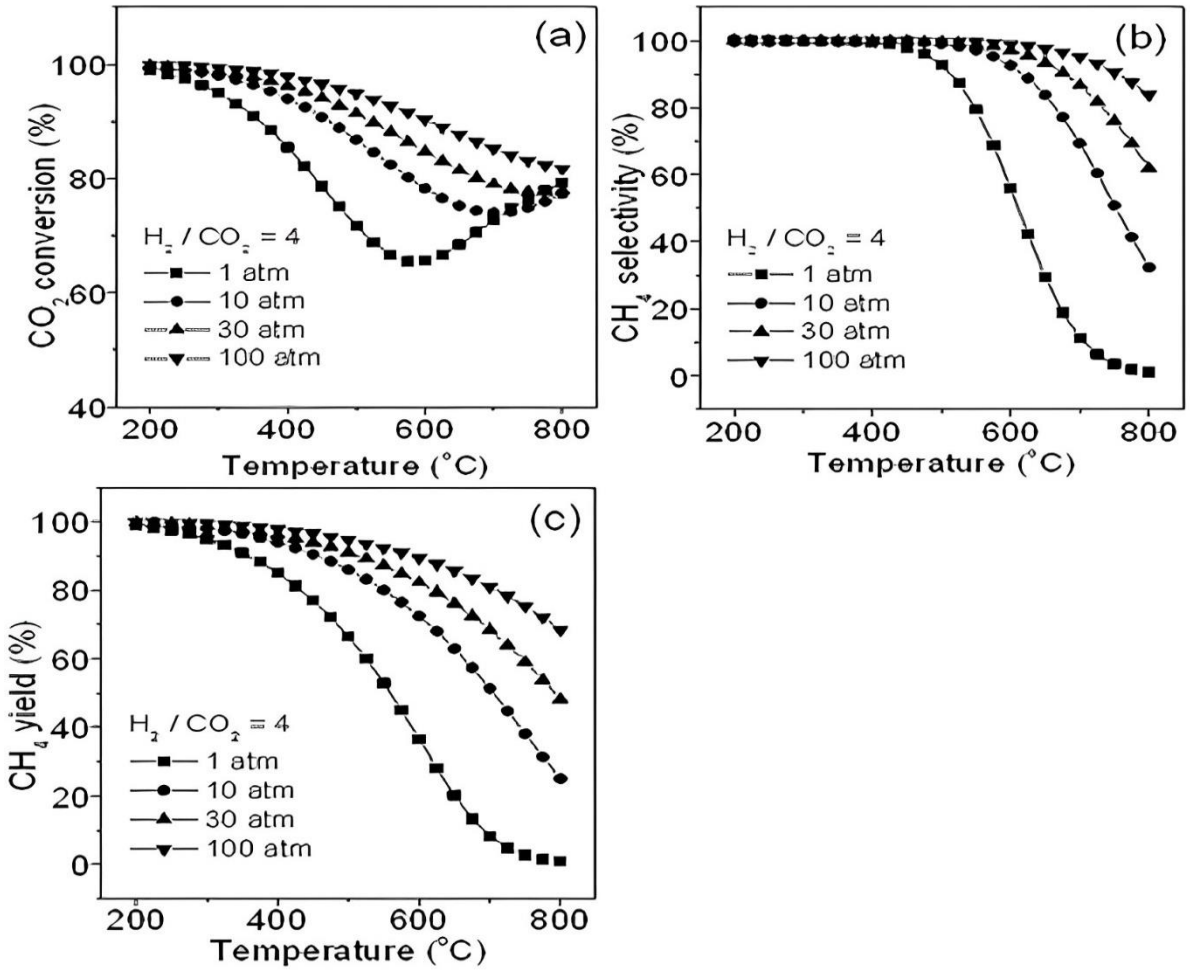

Figure 1: Effects of pressure and temperature on CO_2 methanation: (a) CO_2 conversion, (b) CH_4 selectivity, and (c) CH_4 yield.

The reaction goes from CO methanation (1) to the reverse water-gas shift reaction (2), ending up in CO_2 methanation (3), this last one also known as Sabatier reaction. Note that CO_2 methanation is a linear combination of CO methanation (1) and water-gas shift reaction (2) , this reaction can result in coke formation and low selectivity towards CH_4 [17]. The equilibrium constant is key to the reaction and will depend on the thermodynamic conditions in which the simulations will be carried out.

$$CO+3H_2 \rightleftharpoons CH_4+H_2O \qquad \Delta H_r = -206 \text{ kj/mol (at T=298K)} \qquad (1)$$

$$CO+H_2O \rightleftharpoons CO_2+H_2 \qquad \Delta H_r = -41 \text{ kj/mol (at T=298K)} \qquad (2)$$

$$CO_2+4H_2 \rightleftharpoons CH_4+2H_2O \qquad \Delta H_r = -165 \text{ kj/mol (at T=298K)} \qquad (3)$$

At last, once the reaction is completed, the obtained water will be cooled and condensed to be split and separated from pure methane gas, and closing eventually, the cyclical process to obtain eco-friendly fuel from CO_2. It is key to understand the steps involved in CO_2 methanation and the intermediates formed during the process to a suitable catalyst design and optimization.

The existing reactor concepts methanation can be categorized according to the support material, such as honeycombs or pellets; temperature profile, that can be isothermal, adiabatic or polytropic; and finally, the phases involved in the reaction, which can be single, two, or three phase. According to this classification, the two big concepts currently researched are thermochemical and biochemical reactors [13,50].

Thermochemical reactors require smaller volumes due to its high temperature and reaction rate, but a complete CO2 methanation in a single-phase reactor is difficult because of thermodynamic equilibrium constraints. Their typical operating conditions are pressures from 1 to 100 bar and temperatures from 300ºC to 550ºC. They can be classified into fixed bed methanation, fluidized bed methanation and three phase methanation. Fixed bed methanation plants are ideally almost adiabatic and are the most popular option because of its high reaction rate, where the reactor is filled with millimetric catalyst particles. Its main challenge is the control of temperature and thermodynamic constraints that limit the conversion for temperatures above 300ºC, as well as catalyst deactivation for temperatures above 550-700ºC. Several interesting solutions have been developed, for instance, the TREMP process recovers the heat as high pressure superheated steam [50,51,52]. The fluidized bed reactor is ideally isothermal offering a better heat removal and simpler design, albeit catalyst may be broken during the process as it suffers mechanically and an incomplete conversion can happen because of bubbling, in addition to this, reaction rates are limited due to its isothermal operating conditions (moderate temperatures). Three-phase-methanation reactors, which are also ideally isothermal, outstands for the good heat dissipation and control, but they are difficult to design and operate, as well as its limitation due to the liquid side mass transfer must be taken into consideration [13,50,51]. In the latter case, the liquid phase will influence the effective reaction and its kinetics is mostly determined by the gas concentration in the

liquid [53,54]. Finally, cooled fixed-bed and structured reactors are basically polytropic reactors that combines the advantages of both isothermal and adiabatic reactors, resulting in moderate hot spots and lower outlet temperatures enhancing thoroughly the effectiveness of the reactor. In counterpart to this, they are in general more expensive than adiabatic and isothermal reactors [13,51,60]. For biochemical reactors, transformation of the hydrogen from gas phase to liquid phase limits the mass transfer and hence hinders a good reaction for them. Its main advantage is that can operate at relatively low temperature (40^{o}C to 70^{o}C), and its catalysts (biocatalysts) have demonstrated high tolerance to impurities from feed gas. These characteristics makes it an interesting option for small projects but not for high demanding plants [50]. An overview of established methanation concept will be summarized in the next table 1, 2, 3 and 4 [13,51]:

Table 1: Established methanation concepts for cooled-fixed bed reactors

Cooled fixed-bed methanation		
Creator:	**Technology:**	**Fundamental:**
Linde	/	Cooled reactor with an integrated contorted heat exchanger and an additional adiabatic reactor. Educt gas is added between both reactos.

Table 2: Established methanation concepts for fluidized bed reactors

Fluidized-bed methanation		
Creator:	**Technology:**	**Fundamental:**
Bituminous Coal Research Inc.	Bi-Gas-Process	Fluidized-bed methanation process with internal heat exchangers.
Thyssengas	COMFLUX process	Fluidized-bed reactor concept with internal heat exchanger.

Table 3: Established methanation concepts for three-phase bed reactors

Three-phase methanation		
Creator:	**Technology:**	**Fundamental:**
Chem systems Inc.	Liquid-Phase Methanation (LPM) concept	Single three-phase reactor operated at high pressure and the catalyst suspended in an inert liquid phase

Table 4T: Established methanation concepts for Fixed bed reactors

Fixed-bed methanation		
Creator:	**Technology:**	**Fundamental:**
Air Liquide (Lurgi)	/	Two fixed-bed reactors with intermediate cooling and gas recycling.
Haldor Topsøe	TREMP	3-4 adiabatic fixed-bed reactors focusing on high-temperature methanation
Ralph M. Parsons (RPM)	/	4-7 adiabatic fixed-bed reactors in series that avoids gas recycling and uses intermediate gas coolers and staged gas feed to control temperature
Imperial Chemical Indurstries (ICI) and Koppers	/	Once-through methanation process using several fixed-bed reactors in series with intermediate cooling and steam addition to control temperature
Clariant and Foster Wheeler	Vesta methanation process	3 fixed-bed reactors in series with steam addition for temperature control based on technology from ICI
Johnson Matthey/Davy Technologies	/	3 adiabatic fixed-bed reactors with intermediate gas cooling and recycling based on HICOM methanation
British Gas and Conoco	HICOM (High Combined Shift Methanation)	3 adiabatic fixed-bed reactors with intermediate gas cooling and recycling

However, not all of them are currently commercially available. For CO methanation, available technologies are: Lurgi, TREMP, Clariant and Foster wheeler, Johnson Matthey, and Linde. For CO_2 methanation, the available technologies are from the table 5 below plus the mentioned technologies for CO methanation [13,51].

Table 5: CO_2 methanation technologies available on the market currently

CO_2 methanation technologies available on the market		
Creator:	**Technology:**	**Fundamental:**
Outotec.	Outotec methanation	Staged fixed-bed reactor with intermediate cooling
Etogas	Etogas methanation	Fixed-bed reactor or plate reactor with steam cooling
MAN	MAN methanation	Isothermal fixed-bed reactor with molten salt cooling

With the evolution and higher exigency of the changing energy system, the methanation process needs to be optimized satisfying the new demands, this optimization is primarily focused on temperature control enhancement, cost reduction and improved flexibility of methanation so it can work synchronizing with the fluctuating renewable sources. Fixed bed reactors are the most researched with great difference and a large quantity of adiabatic or cooled fixed-bed reactors are used in this sense. Structured reactors are being investigated to overcome drawbacks of adiabatic reactors such as honeycomb reactors, micro-structured reactors or sorption-enhanced reactors. As for fluidized-bed reactors, the Chinese Academy of Sciences is developing a specially designed catalyst to tackle the mechanical-stress problem of the catalyst. The Paul Scherrer Institute (PSI) is demonstrating the CO methanation derived from biomass gasification with the construction of a fluidized-bed methanation reactor that will be enhanced with another pilot plant in Switzerland. Additionally, the Engie Gas company is also trying to realize Power-to-Gas demonstration with biomass gasification and methanation. Finally, Götz et al. is investigating hydrodynamics and heat transfer fluid stability to enhance the performance of three-phase methanation reactors. An optimized catalyst is also being developed for this type of reactors in the Key Laboratory of Coal Science and Technology of Taiyuan in China [13,51].

On the other hand, a number of long duration tests were conducted to demonstrate the technical feasibility of direct methanation of real biogas, utilizing various reactor concepts including fluidized bed, by Witte et al, micro-structured heat exchange reactor by Guilera et al., and cooled fixed bed, by Specht et al. The volume of these reactors varies from few liters (catalytic) to cubic meters (biological), an outperformance in favor of catalytic reactors has been observed, nonetheless biological reactors are economically more practical [13,51].

Whilst SNG production from coal has a long history, production from renewable sources such as solar or wind waste energy or biomass are comparatively shorter. However, due to increasing importance of sustainability, they possess a very attractive and promising approach, nonetheless they create new challenges that makes profitable methanation difficult. Fortunately, they are currently under wide investigation, with various reactor concepts in Europe [61,62,63], or innovative methanation process designs. For instance, the Energy Research Center of the Netherlands (ECN) has developed a general concept that includes biomass gasification in a dual fluidized bed gasifier called MILENA [64], the Center for Solar

Energy and Hydrogen Research (ZSW) has developed the Absorption Enhanced gasification/Reforming (AER) [65], Paul-Scherrer Institut (PSI) has carried out a research converting dry biomass to SNG in collaboration with Gazhobois SA and École Polytechnique Fédérale de Lausanne (EPFL). Other recent interesting and highly innovative projects can be found in [13,51,66,67,68,69,70,71], the majority of them are biomass/coal based methanation.

2.2 REACTION KINETICS

ADDmeth is a polytropic air-cooled fixed bed reactor and will run as a pseudohomogeneous, continuous reactor in Ansys fluent for time-efficiency reasons [18]. The models that can be used are in constant research and a large number of them have been developed over the past forty years [19]. Most nickel-based kinetic models follow the Langmuir-Hinshelwood-Hougen-Watson (LHHW) approach, whose basic structure is shown in eq.4, and then modified with experimental data to determine its definitive equations and kinetic parameters [20]. This approach is used for reactions that occur at the surface area and the existing porous inner space of the catalyst.

$$r = \frac{(kinetic\ factor)\cdot(driving\ force)}{(adsorption\ expression)^n} \qquad (4)$$

Nevertheless, only few models can provide the fixed bed reactors simulations with sufficiently wide temperature and pressure range. In this work, the most relevant and commonly applied will be chosen and compared, overviews are given in [20,21,22] and table 6:

Table 6: Overview of most used kinetic models

Kinetic Model	Ni Content Catalyst	Catalyst	Reactions
Xu and Froment	15 wt%	$Ni/MgAl_2O_3$	CO, CO_2, WGS
Kopycinski	50 wt%	Ni/Al_2O_3	CO (not backwards), WGS
Zhang et al.	50 wt%	Ni/Al_2O_3	CO (not backwards)
Klose and Baerns	18 wt%	Ni/Al_2O_3	CO (not backwards)
Koschany et al.	25 wt%	Ni/Al_2O_3	CO_2

The model from Xu and Froment is widely followed but is limited by the catalyst used and a narrow reaction condition [13,23], additionally, it was created to measure methane steam reforming and the rates below 700K were almost inactive [20,23]. Kopyscinski's model was designed for fluidized-bed, quasi-isothermal reactor with temperatures around 300 °C, and performed a methane reforming that was too intensive [13,20,26]. Klose and Baerns developed a CO methanation model with an 18 wt% Ni/Al_2O_3 in a Berty reactor [18,20,24]. Koschany's model was recommended by Scharl et al. for dynamic simulations although it only takes CO_2 methanation into account [18,25]. Zhang adopted the models from Xu and Klose using a 50 wt% Ni/Al_2O_3 as well as considering the reverse water-gas shift reaction. Moreover, the rates showed by Zhang's model was more suitable than Xu and Kopyscinski's models in recent studies [13,27]. Finally, Rönsch et al. recommended the models of

Zhang and Klose for dynamic simulations that covers considerable range of temperature and pressure range by adding to them a term for reverse reaction, which ends up in methane reforming at a higher temperature [13,18].

In this project, the model from Zhang et al. with adjustment of Rönsch et al. will be the chosen one to run calculations as it has the possibility to dynamic modelling and offers a wide temperature range, along with pressure range, allowing more freedom while experimenting. The model uses a nickel-based catalyst whose reacting surface is improved with alumina (Al_2O_3), resulting in a commercial Ni/Al_2O_3. The model is based on the following equations that correspond to CO methanation (5) and reverse water-gas shift reaction (6).

$$r_1 = \frac{k_1 * K_C * K_H^2 * \left(p_{CO}^{0.5} * p_{H_2} - \frac{p_{CH_4} * p_{H_2O} * p_{CO}^{-0.5} * p_{H_2}^{-2}}{K_{Meth}} \right)}{(1 + K_C * p_{CO}^{0.5} + K_H * p_{CO}^{0.5})^3} \quad (5)$$

$$r_2 = \frac{\frac{k_2}{p_{H_2}} * \left(p_{CO} * p_{H_2O} - \frac{p_{H_2} * p_{CO_2}}{K_{WGS}} \right)}{\left(1 + K_{CO} * p_{CO} + K_{H_2} * p_{H_2} + K_{CH_4} * p_{CH_4} + K_{H_2O} * p_{H_2O} * p_{H_2}^{-1}\right)^2} \quad (6)$$

Their parameters are listed in the table below (Table7):

Table 7: Parameters for the kinetic model of Zhang et al. with adjustments of Rönsch et al. from literature [74].

Parameter	Original data with transformed dimensions	Unit
$\boldsymbol{k_1}$	$1.94 * 10^7 * \exp\left(-\frac{103000 J/mol}{RT}\right)$	$\left[\frac{kmol}{kg_{cat} * s}\right]$
$\boldsymbol{k_1^* = k_1 * K_C * K_H^2}$	$9.13 * 10^{-8} * \exp\left(-\frac{29000 J/mol}{RT}\right)$	$\left[\frac{kmol * Pa^{-1.5}}{kg_{cat} * s}\right]$
$\boldsymbol{k_2}$	$2.18 * 10^{-2} * \exp\left(-\frac{62000 J/mol}{RT}\right)$	$\left[\frac{kmol * Pa^{-1}}{kg_{cat} * s}\right]$
$\boldsymbol{K_C}$	$1.83 * 10^{-6} * \exp\left(\frac{42000 J/mol}{RT}\right)$	$[Pa^{-0.5}]$
$\boldsymbol{K_H}$	$5.06 * 10^{-5} * \exp\left(\frac{16000 J/mol}{RT}\right)$	$[Pa^{-0.5}]$
$\boldsymbol{K_{CO}}$	$8.23 * 10^{-10} * \exp\left(\frac{70650 J/mol}{RT}\right)$	$[Pa^{-1}]$
$\boldsymbol{K_{H_2}}$	$6.12 * 10^{-14} * \exp\left(\frac{82900 J/mol}{RT}\right)$	$[Pa^{-1}]$
$\boldsymbol{K_{CH_4}}$	$6.65 * 10^{-9} * \exp\left(\frac{38280 J/mol}{RT}\right)$	$[Pa^{-1}]$
$\boldsymbol{K_{H_2O}}$	$1.77 * 10^5 * \exp\left(-\frac{88680 J/mol}{RT}\right)$	
$\boldsymbol{\frac{1}{K_{Meth}}}$	$1.027 * 10^{10} * \exp\left(30.11 - \frac{26830}{T}\right)$	$[Pa^2]$
$\boldsymbol{\frac{1}{K_{WGS}}}$	$\exp\left(4.063 - \frac{4400}{T}\right)$	
[a]C = 0 and D = 0 for all parameters.		

Where k_i (i=1,2) is a rate coefficient and K_j (j=C,H,CO,H_2,CH_4,H_2O) is an adsorption constant. These parameters are defined as temperature functions based on Arrhenius equation (7) and Van't Hoff equation (8). The use of catalyst will cause changes to the activation energy and its related reaction rates (the activation energy of Arrhenius equation), hence an adequate kinetic model based on the specifically used catalyst is needed. E_A (J/mol) is defined as activation energy, ΔH_{Ads} (J/mol · K) as adsorption heat of the species, R (J/mol · K) as the universal constant of ideal gas, and finally T (K) as temperature.

$$k_i = k_i^0 * \exp\left(-\frac{E_{A,i}}{RT}\right) \qquad (7)$$

$$K_j = k_j^0 * \exp\left(-\frac{\Delta H_{Ads,j}}{RT}\right) \qquad (8)$$

And their parameters are given in the following (table 8), note that $k_{0.1(18wt\%)}$ and $k_{0.1(50wt\%)}$ shall be used depending on the catalyst used.

Table 8: kinetic parameters from Rönsch et al. [20]

Parameter	Value	Unit
$k_{0,1(18wt\%)}$	$(4.8/3.6) * 10^9$	$[mol\ kg^{-1}\ cat\ s^{-1}]$
$k_{0,1(50wt\%)}$	$(7.0/3.6) * 10^{10}$	$[mol\ kg^{-1}\ cat\ s^{-1}]$
$k_{0,2}$	$(7.83/3.6) * 10^6$	$[mol\ kg^{-1}\ cat\ s^{-1}\ bar^{-1}]$
$E_{A,1}$	103000	$[J\ mol^{-1}]$
$E_{A,2}$	62000	$[J\ mol^{-1}]$
$K_{0,C}$	$5.8 * 10^{-4}$	$[bar^{-0.5}]$
$K_{0,H}$	$1.6 * 10^{-2}$	$[bar^{-0.5}]$
$K_{0,CO}$	$8.23 * 10^{-5}$	$[bar^{-1}]$
K_{0,H_2}	$6.12 * 10^{-9}$	$[bar^{-1}]$
K_{0,CH_4}	$6.65 * 10^{-4}$	$[bar^{-1}]$
K_{0,H_2O}	$1.77 * 10^5$	$[-]$
$\Delta H_{Ads,C}$	-42000	$[J\ mol^{-1}]$
$\Delta H_{Ads,H}$	-16000	$[J\ mol^{-1}]$
$\Delta H_{Ads,CO}$	-70650	$[J\ mol^{-1}]$
$\Delta H_{Ads,H_2}$	-82900	$[J\ mol^{-1}]$
$\Delta H_{Ads,CH_4}$	-38280	$[J\ mol^{-1}]$
$\Delta H_{Ads,H_2O}$	88680	$[J\ mol^{-1}]$

K_{Meth} is the equilibrium constant of CO methanation and K_{WGS} the equilibrium constant of water-gas shift. These 2 parameters can be calculated by Elnashaie (9) and Elshishini (10) equations [28].

$$K_{Meth} = \frac{1}{1.026676 * 10^{10}} * \exp\left(\frac{26830K}{T} - 30.11\right) \qquad (9)$$

$$K_{WGS} = \exp\left(\frac{4400K}{T} - 4.063\right) \qquad (10)$$

2.3 COMPUTATIONAL FLUID DYNAMICS (CFD)

When a fluid gets the fundamental laws of mechanics applied, it will obtain a set of coupled non-linear partial differential equations as a consequence, that are hard and time-consuming to resolve manually. CFD is a valuable computational tool that solves and approximates these differential equations using numerical methods within a defined flow geometry. The resolution will consider physical characteristics of fluid such as conservation of energy, matter, momentum, etc. Moreover, appropriate initial and boundary conditions must be applied to solve adequately the Navier-Stokes equations and the continuity equations, which are the fundamental equations of fluid dynamics. With the development of high-speed and large memory computers CFD has been able to tackle a significant number of flow-related problems and hence being crucial to multiple industries such as aerospace, energy, nuclear and chemical [29,30].

The Navier-Stokes equations consists of four equations. One of them is the mass increase rate at a given point, in differential form, shown as below (11):

$$\frac{\partial \rho}{\partial t} + \frac{\partial}{\partial x}(\rho u) + \frac{\partial}{\partial y}(\rho v)\frac{\partial}{\partial z}(\rho w) \qquad (11)$$

The other 3 equations can be obtained by deriving the equation of conservation of momentum, that is the same as Newton's second law (12). There will be three components due to momentum is a vector quantity, each component will generate one equation resulting in 3 different and independent equations that represent one direction (13,14,15).

$$F = ma \qquad (12)$$

$$\frac{\partial(\rho u)}{\partial t} + \frac{\partial(\rho u^2)}{\partial x} + \frac{\partial(\rho uv)}{\partial y} + \frac{\partial(\rho uw)}{\partial z} = -\frac{\partial p}{\partial x} + \frac{\partial}{\partial x}\left(\lambda \nabla * \vec{V} + 2\mu \frac{\partial u}{\partial x}\right) + \frac{\partial}{\partial y}\left[\mu\left(\frac{\partial v}{\partial x} + \frac{\partial u}{\partial y}\right)\right] + \frac{\partial}{\partial z}\left[\mu\left(\frac{\partial u}{\partial z} + \frac{\partial w}{\partial x}\right)\right] + \rho f_x \qquad (13)$$

$$\frac{\partial(\rho v)}{\partial t} + \frac{\partial(\rho uv)}{\partial x} + \frac{\partial(\rho v^2)}{\partial y} + \frac{\partial(\rho vw)}{\partial z} = -\frac{\partial p}{\partial y} + \frac{\partial}{\partial x}\left[\mu\left(\frac{\partial v}{\partial x} + \frac{\partial u}{\partial y}\right)\right] + \frac{\partial}{\partial y}\left(\lambda \nabla * \vec{V} + 2\mu \frac{\partial v}{\partial y}\right) + \frac{\partial}{\partial z}\left[\mu\left(\frac{\partial w}{\partial y} + \frac{\partial v}{\partial z}\right)\right] + \rho f_y \qquad (14)$$

$$\frac{\partial(\rho w)}{\partial t} + \frac{\partial(\rho uw)}{\partial x} + \frac{\partial(\rho vw)}{\partial y} + \frac{\partial(\rho w^2)}{\partial z} = -\frac{\partial p}{\partial y} + \frac{\partial}{\partial x}\left[\mu\left(\frac{\partial u}{\partial z} + \frac{\partial w}{\partial x}\right)\right] + \frac{\partial}{\partial y}\left[\mu\left(\frac{\partial w}{\partial y} + \frac{\partial v}{\partial z}\right)\right] + \frac{\partial}{\partial z}\left(\lambda \nabla * \vec{V} + 2\mu \frac{\partial w}{\partial z}\right) + \rho f_z \qquad (15)$$

These 4 equations form the generic form of the renowned Navier-Stokes equation. This generic form can then be expanded to form the energy conservation equation, mass conservation equation and momentum conservation equation [29,31]

Solving these equations analytically is currently almost impossible to scaled-up applications, thus numerical solutions are needed. CFD will replace the differential equations with algebraic equations by discretization, obtaining a result that will be similar to the actual solution [29,31,32]. The main discretization methods are: Finite element method [33], Finite volume method [34] and Finite difference method [35], [29,32]. The following figure compares the actual solution to the CFD numerical solution (Fig.2):

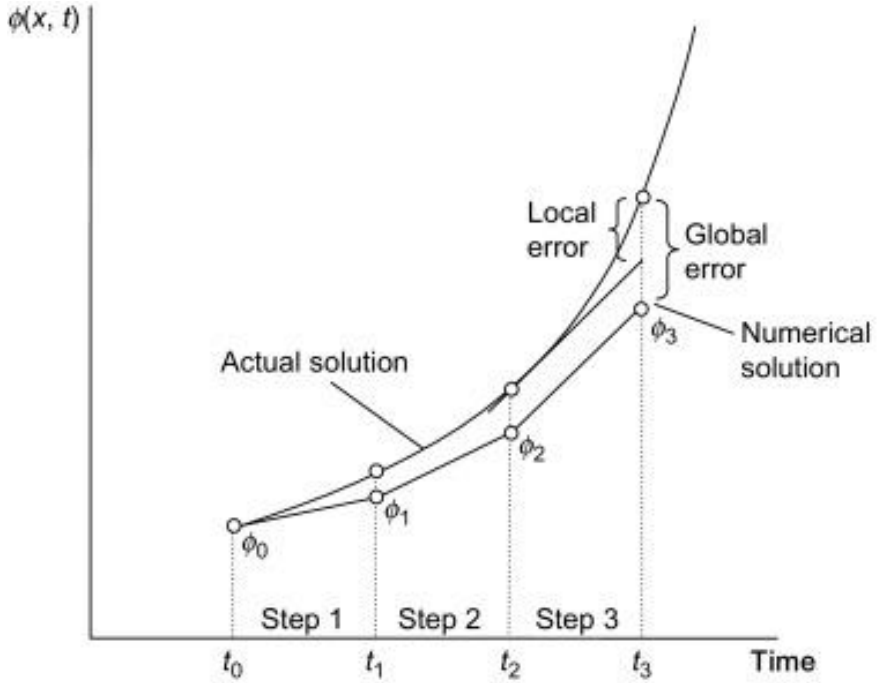

Figure 2: Comparison between Numerical and actual solution [73]

3.METHODOLOGY

The first step is to define all the relevant parameters and geometries for the problem. In this case, the reactor will be two-dimension and will be designed and drawn with "CATIA V5". The parameters will be inserted into CFD with the so-called "Used Defined Memory", which is a C code that includes the kinetic model explained in the previous section, this code will be explained in a latter section. The result geometry follows as shown (Fig.3):

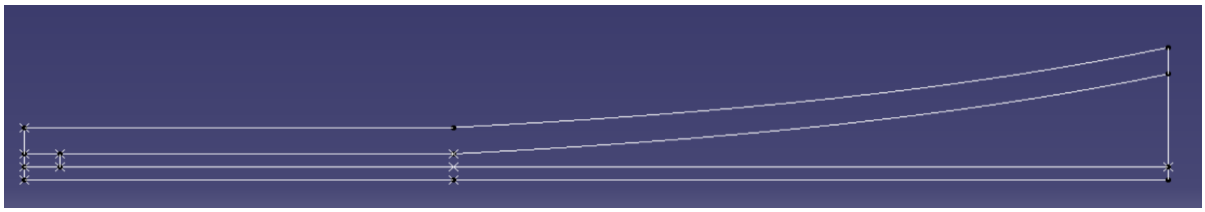

Figure 3: The model of the reactor seen from Catia V5.

This design is a computational adaptation of the physical reactor presented in [9], and its dimensions are as follows (Fig.4):

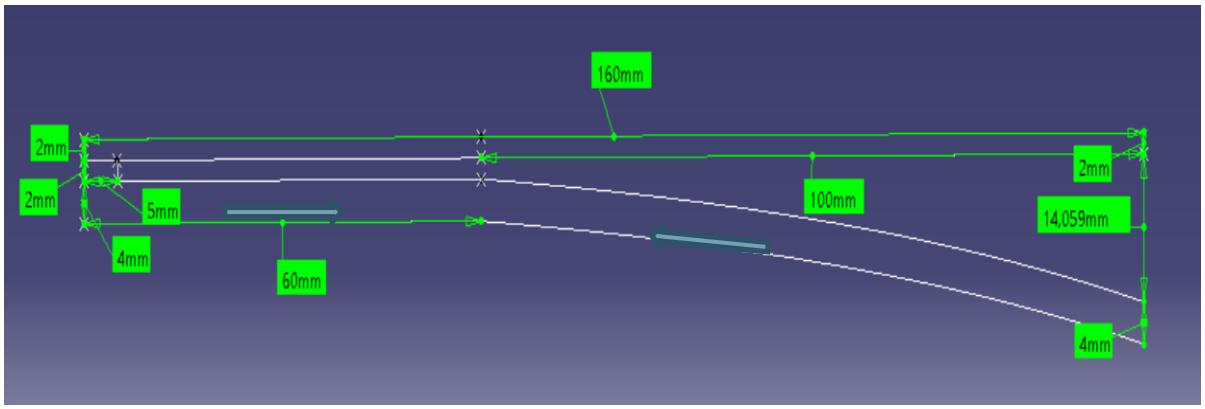

Figure 4: Dimensions of the reactor.

The conical curve of the reactor should initially follow the next equation (16):

$$y = 3.6997 * e^{(0.0146*x)} + 4 \qquad (16)$$

This equation was obtained from excel after parametrization of the geometry (Tab.9), and then applying exponential trendline and showing the equation (Fig.5):

Table 9: experimental data used to obtain the conic curve.

X (cm)	Y (cm)
0	4
10.17	4.29
20.94	4.84
30.79	5.56
39.9	6.4
50.41	7.58
60.26	8.88
70.61	10.45
80.52	12.15
90.56	14.04
100	16

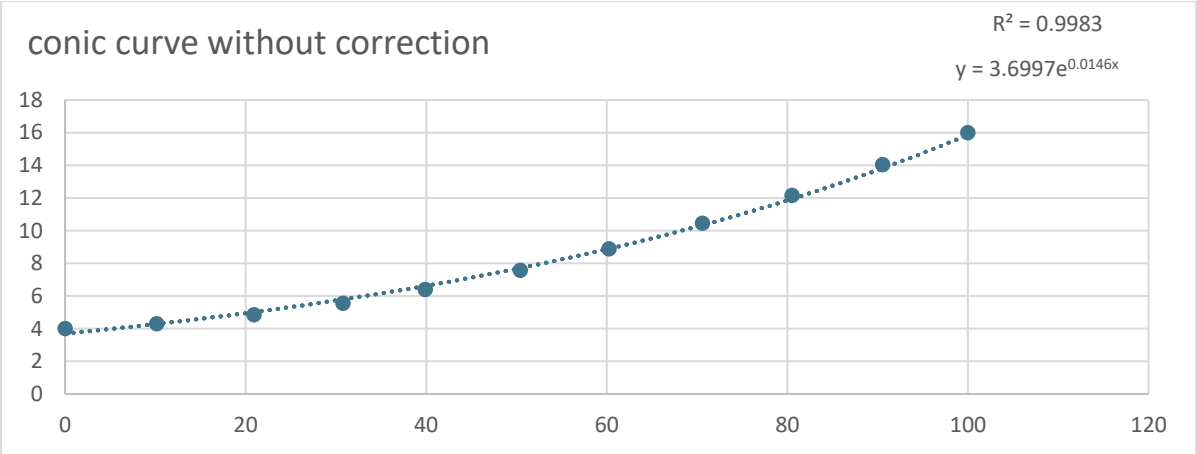

Figure 5: First equation obtained from experimental data with errors.

However, this trendline has some errors (Fig. 6) and needs to be corrected manually: the x-label must start from 0cm to 100cm as it the length of the horizontal parallel curve, and the y-label must be between 4cm-16cm as it is the length of the diameter, without counting the wall of the reactor (indicated with orange arrows in Fig.11). The corrected equation will be (17):

$$y = 4 * \exp(0.0139 * x * 100) \qquad (17)$$

The factor multiplying to the exponential must be 4, as y-label starts from 4cm reading from figure 12, and then it must multiply to a hundred to shift from centimeters to millimeters. This is because the model drawn in CATIA V5 works with millimeters.

Figure 14 shows how the corrected formula has a better R square value of exactly 1, and how it coincides perfectly with the scatter points:

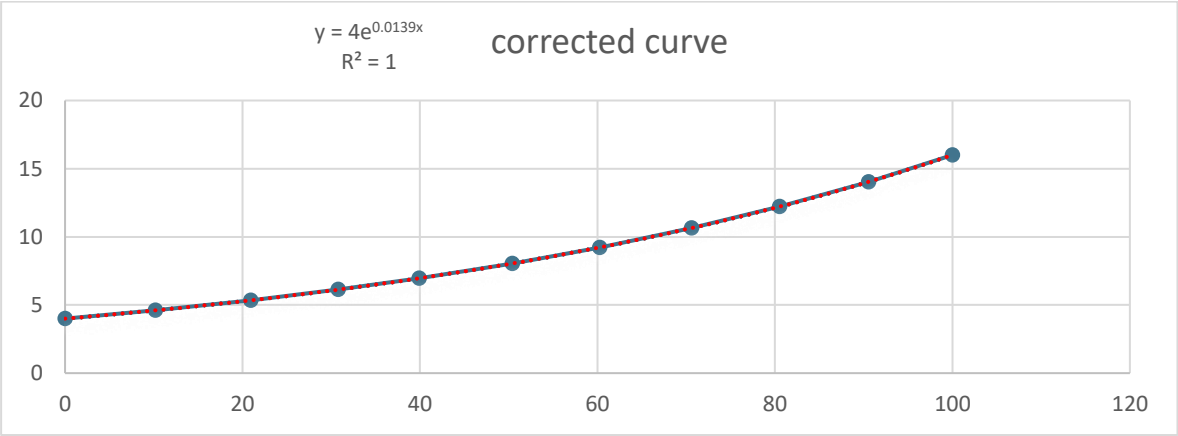

Figure 6: Corrected curve

The conic curve parallel and down to the first conic curve follows the next equation (18):

$$y = 4 * \exp(0.0139 * x * 100) + 4 \qquad (18)$$

Note that only difference is the sum 4, as the discussed curve is exactly 4 centimeters below the first conic curve.
A more detailed view of the inlet (Fig.7) and outlet (Fig.8) can be seen in the following figures:

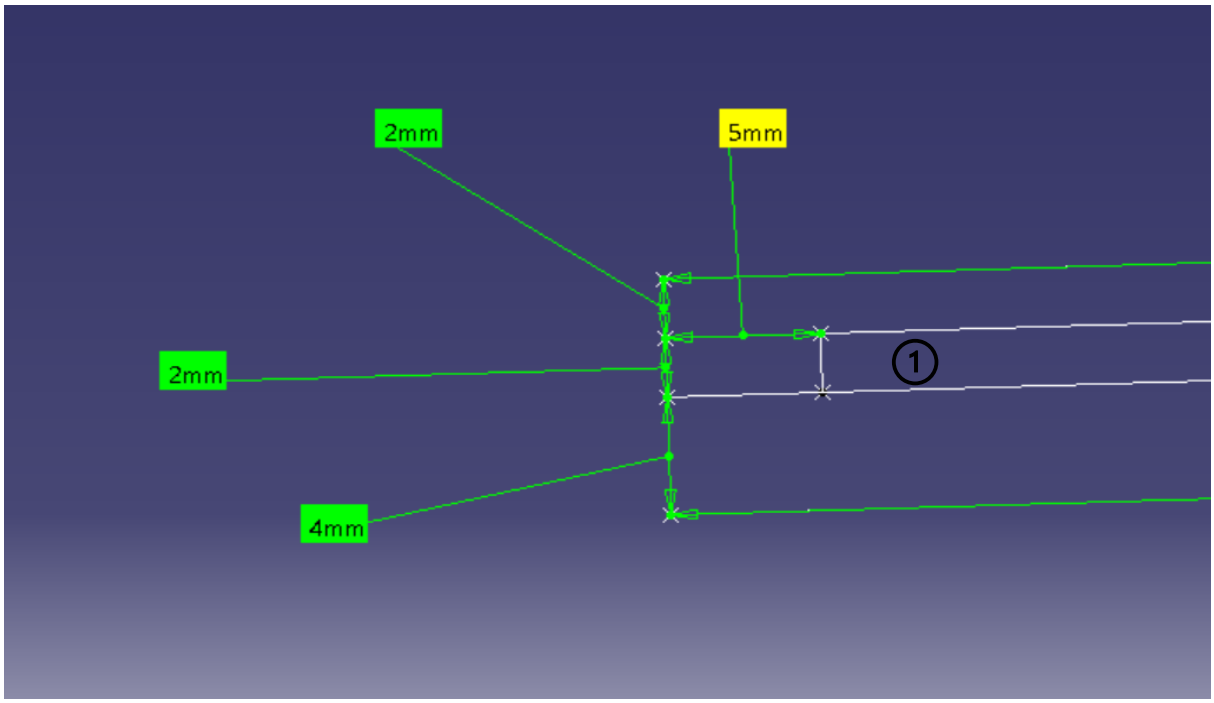

Figure 7: dimensions of the inlet.

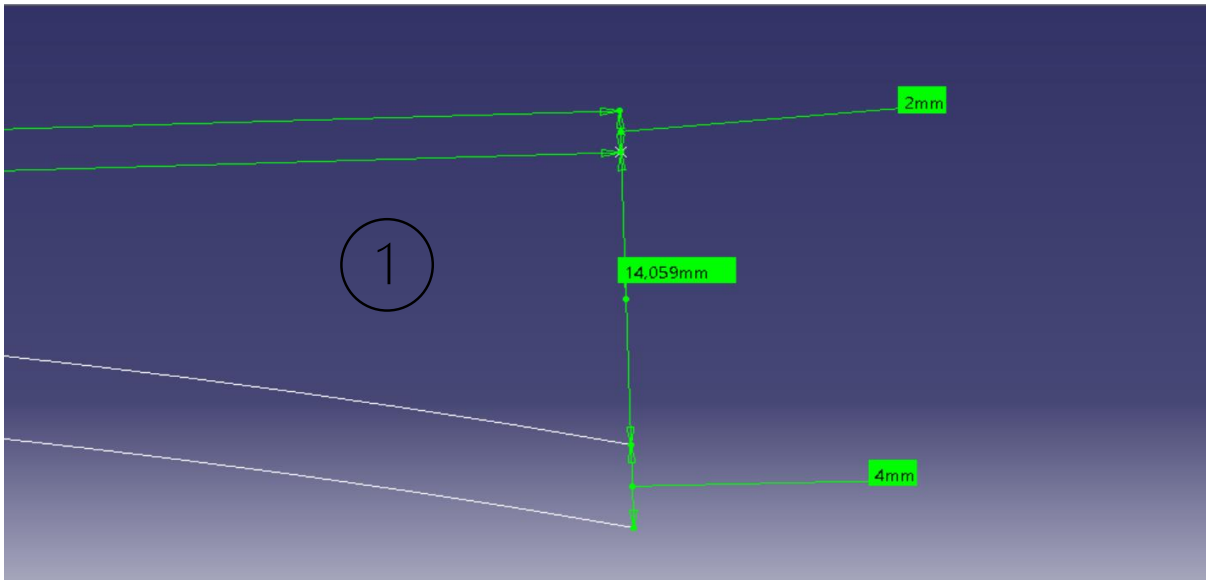

Figure 8: dimensions of the outlet.

Note how the reacting zone (marked with ①) expands from 2mm to 14.059mm, which is assumed to be 14mm. But the rest is maintained constant.

The second step is the construction of mesh that represents the physical environment in which the simulation will occur, it is therefore here, where the reactor will be divided into different parts to set up boundary conditions later. This mesh is the computational geometric domain of the reactor that is formed by smaller discrete

cells. Each cell will solve the CFD equations independently and eventually approximate the solution over the larger domain. Consequently, the larger the number of cells the more accurate the calculation will be, but the operational time will also soar quickly. This process will be done within “Ansys ICEM”. This step must be done with carefulness to ensure high quality of the mesh, if this quality is not good enough the results will not be close to reality. The resulting mesh is shown in figure 10. The parts are as shown in the following figure (figure 9):

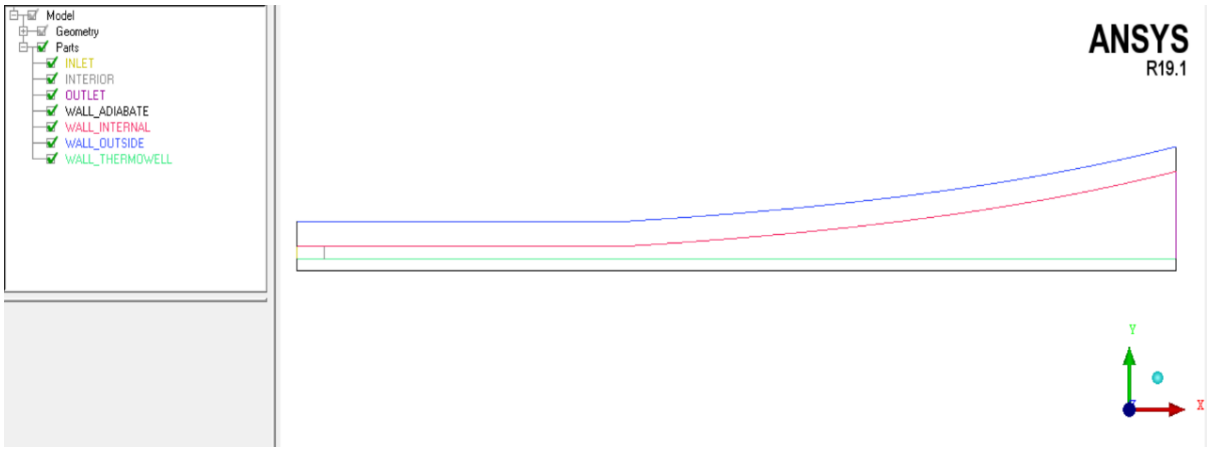

Figure 9: Parts of the reactor

The parts are associated with their corresponding color: dark yellow for inlet; grey for interior; purple for outlet; black for adiabatic walls; red for internal wall; blue for outside wall and finally green for thermowell wall.

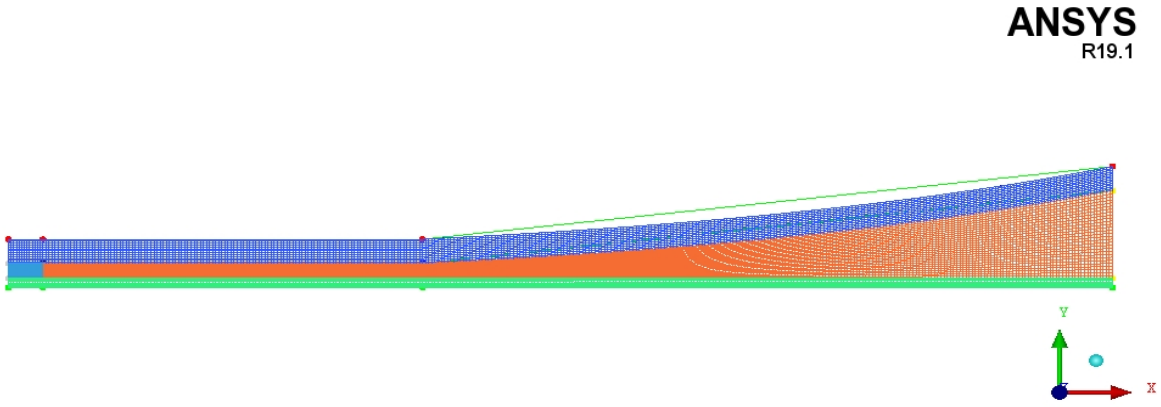

Figure 10: meshing of the reactor.

Reading from Figure 10, the reactor has been split into 4 zones: orange zone represents the reaction zone; navy blue zone represents the steel wall of the reactor; light blue zone represents the inert zone, where no reaction has been taken place; and finally green zone represents the thermowell. This mesh contains a total of 13398 cells (basic cell size: 1).

Finally, the mesh drawn on ICEM will be imported into “Ansys Fluent”, all the parameters and configurations, as well as the boundary conditions will be defined here, and after their readiness, the calculation will start to run.

3.1 Configuration of the Reactor and Boundary Conditions

For the model configurations, the energy equations are turned on and the viscous model will be laminar, as the Reynolds number is assumed to be small, this means that pressure loss due to turbulence will be low and hence, lower energy losses will be achieved [41]. Additionally, internal mass transport as well as heat exchange must be considered when modelling methanation reactors [18, 36]. Species transport will be enabled along with diffusion energy source. The species considered are CO_2, CO, H_2O, H_2, CH_4, N_2 and the mixture properties for the mixture template are given in the following table 10:

Table 10: Values for the mixture properties

Property	Value
Density (kg/m^3)	Ideal gas
Cp (J/kg-K)	Mixing-law
Thermal conductivity (W/m-K)	0.125, constant
Viscosity (Kg/m-s)	1.72e-05, constant
Mass diffusivity (m^2/s)	2.88e-05, constant-dilute-approximation

For material configuration, the following materials are considered: air, carbon-dioxide, carbon-monoxide, hydrogen, methane and oxygen for fluid: aluminum, nial50, steel for solid; carbon-dioxide, carbon-monoxide, water-vapor, hydrogen, methane, nitrogen for mixture template. The mentioned nial50 is the catalyst formed with 50% nickel and 50% alumina. The parameters are given in the table 11, 14 and 15 respectively:

Table 11: Parameters for fluids.

Material/Property	Density(Kg/m3)	Cp(J/Kg-K)	Ther.Cond.(W/m-K)	Viscosity (Kg/m-s)	Molecular weight(Kg/Kmol)
Air	1.225	1006.43	0.0242	1.7894e-05	28.966
CO_2	1.7878	Piecewise-polynomial	0.0145	1.37e-05	44.00995
CO	1.1233	Piecewise-polynomial	0.025	1.75e-05	28.01055
H_2	0.08189	Piecewise-polynomial	0.167291	8.411e-06	2.01594
CH_4	0.6679	Piecewise-polynomial	0.0332	1.087e-05	16.04303
O_2	1.2999	Piecewise-polynomial	0.0246	1.919e-05	31.9988

All values are constant except Cp for CO_2, CO, H_2, CH_4, O_2, that are piecewise-polynomial, these polynomials are mathematical functions used to solve complex differential equations and are crucial to the finite element method, as they represent an approximate solution within each element of the domain. They are defined as multiple different polynomial functions on different intervals instead of one general function describing the entire general domain [37]. They are introduced as follow (table 12, table 13):

Table 12: Piecewise-polynomial profile of Cp of the used materials

Material/Profile	Range	Minimum	Maximum	Coefficients	In terms of (2ranges for all)
CO_2	1	300	1000	5	Temperature
CO	1	300	1000	5	Temperature
H_2	1	300	1000	5	Temperature
CH_4	1	300	1000	5	Temperature
O_2	1	300	1000	5	Temperature

Table 13: Coefficients for the Cp of the piecewise-polynomial profile for the used materials

Material/Coefficients	1	2	3	4	5
CO_2	429.9289	1.874473	0.001966485	1.297251e-06	3.999956e-10
CO	968.3899	0.4487877	0.001152217	1.656882e-06	7.34637e-10
H_2	13602.45	3.402317	0.003358423	3.907953e-07	1.705345e-09
CH_4	403.5847	9.057335	-0.01442509	1.580519e-05	6.343051e-09
O_2	834.8265	0.292958	0.0001495637	3.413885e-07	2.278359e-10

Table 14: Parameters for solids.

Material/Property	Density(Kg/m3)	Cp(J/Kg-K)	Thermal Conductivity (W/m-K)
Aluminum	2719	871	202.4
NiAl50	6429	670	3.176
Steel	8030	502.48	16.27

To calculate the thermal conductivity for the catalyst: NiAl50 is assumed as a open-cell metal foam catalyst in this case. This type of catalyst offers higher porosity, surface area and thermal conductivity in comparison to other traditional catalysts [40]. Its structure is basically a foam that is a pentagonal rotation ellipsoid with cell windows, and its density, in addition to the strength of the matrix material and the shape of cellular structure, are the main reasons characterizing the mechanical properties of the catalyst. Its distribution of mass is almost isotropic since it is a network-like structure, this makes its thermal conductivity also fairly isotropic through all the material, the heat transfer coefficient will be mainly influenced by the cell diameter and porosity [41,42]. In this case, the effective foam thermal conductivity, λ_{eff} can be estimated using various correlations and methods, but the simplest equation, that is based on asymptotic solutions, will be as follow (19):

$$\lambda_{\text{eff,parallel}} = \varepsilon\, \lambda_{fluid} + (1-\varepsilon)\lambda_{solid} \qquad (19)$$

Where the thermal resistance of fluid (λ_{fluid}) and solid (λ_{solid}) phases are mixed in parallel mode upon weighted by the foam porosity [40], represented by ε. λ_{solid} should be initially 30, but since the heat transfer performance will be worsen because of the high temperature, it will be set as 10 in this case. On the other hand, λ_{fluid} will be 0.125 [43,40,44]. In this context, the first value obtained to give place the first scenario is 3.176. Following values will be lower than this trying to observe and

recognize a possible pattern in the results, they are: 2.56 and 1.65. The reaction rate will be 0.0005 fixed and the fixed geometry will follow equations 17 and 18.

Table 15: Parameters for mixture template materials.

Material/Property	Cp(J/Kg-K)	Molecular weight(Kg/Kmol)
Water-Vapor	Piecewise-polynomial	18.01534
CO_2	Piecewise-polynomial	44.00995
CO	Piecewise-polynomial	28.01055
H_2	Piecewise-polynomial	2.01594
CH_4	Piecewise-polynomial	16.04303
N_2	Piecewise-polynomial	28.0134

The Cp piecewise-polynomial profile for the materials on table 15 are the same as stated in table 12, the coefficients for CO_2, CO, H_2, CH_4, are the same to the table 13, and the coefficients for N_2 and water-vapor are as follow (table 16):

Table 16: Coefficients for the Cp of the piecewise-polynomial profile for water-vapor, nitrogen.

Material/Coefficients	1	2	3	4	5
Water-vapor	1563.077	1.603755	0.002932784	3.216101e-06	1.156827e-09
N_2	979.043	0.4179639	0.001176279	1.674394e-06	7.256297e-10

The next step is to set up cell zone conditions: the inert zone is a fluid defined as a porous zone with a Viscous Resistance of 3.292181e+08 m^{-2} in both directions (1 and 2) as a constant. The Inertial Resistance will be 3111 m^{-1} in both directions (1 and 2) as a constant. The porosity is set as 0.36, with the Thermal Model in equilibrium, and the Relative Viscosity is constant. Finally, the Solid material is NiAl50. The reaction zone is also a fluid set as a porous zone with the exact same properties as the inert zone with the only difference of the source terms being loaded here. The rest is configured as predetermined.

After parametrizing cell conditions, the subsequent step is to introduce values for boundary conditions on the different reactor parts, the name of the parts are loaded automatically when reading the mesh from ICEM in Fluent. The inlet is defined as velocity-inlet with the following configurations (table 17):

Table 17: configuration for inlet

Momentum	Thermal	Species
Velocity specification Method: Magnitude, Normal to Boundary	Temperature (K):565, constant	Species are specified in Mole Fractions
Reference Frame: Absolute		Species Mass Fractions (all 0 except for CO_2 and H_2):
Velocity magnitude (m/s): 1.067, constant		CO_2:0.185, constant
Supersonic/ Initial Gauge Pressure (pascal):0, constant		H_2:0.815, constant

The outlet is defined as Pressure-Outlet and the next parameter configurations have been applied (table 18):

Table 18: configuration for outlet

Momentum	Thermal	Species
Backflow Reference Frame: Absolute	Backflow Total Temperature (k): 300, Constant	0 for all
Gauge pressure (pascal):810600, constant		
Pressure Profile Multiplier: 1		
Backflow Direction Specification Method: Normal to Boundary		
Backflow Pressure Specification: Total Pressure		

For Adiabatic and Internal walls (table 19):

Table 19: configuration for adiabatic walls

Part/Config.	Thermal conditions	Material Name	Heat flux(W/m^2)	Heat generation rate (W/m^3)	Wall Thickness (mm)
Adiabatic wall	Heat Flux	steel	0	0	0
Adiabatic wall 002	Heat Flux	Aluminum	0	0	0
Wall Internal	Coupled	Steel	/	0	0
Wal internal 003	Coupled	Aluminum	/	0	0

The outside wall is understood as Temperature for thermal conditions, its material is steel, and the temperature will be 591K, constant. Last but not least, the thermowell walls will be follow the next configurations (table 20):

Table 20: configuration for thermowell walls

	Wall Thermowell	Wall Thermowell 004
Momentum	Wall motion: Stationary Wall; Shear condition: No Slip	Wall motion: Stationary Wall; Shear condition: No Slip
Thermal	Thermal conditions: Coupled; Material Name: Steel; Wall thickness: 0mm; Heat Generation Rate: 0 W/m^3, constant	Thermal conditions: Coupled; Material Name: Steel; Wall thickness: 0mm; Heat Generation Rate: 0 W/m^3, constant
Species	Zero Diffusive Flux	Zero Diffusive Flux

It is also important to have reference values defined correctly, the reference zone will be the inert zone (table 21):

Table 21: Reference values

Area (m^2)	1
Density (Kg/m^3)	1.225
Depth (m)	1
Enthalpy (j/kg)	0
Length (mm)	1000
Pressure (pascal)	0
Temperature (k)	288.16
Velocity (m/s)	1
Viscosity (kg/ms)	1.7894e-05
Ratio of Specific Heats	1.4

The solution methods are crucial as it will directly influence the results, they vary depending on the material and the parameter discussed (table 22):

Table 22: Solution methods

Scheme	Simple
Gradient	Least Squares Cell Based
Pressure	Standard
Density	First Order Upwind
Momentum	First Order Upwind
CO_2	First Order Upwind
CO	First Order Upwind
H_2O	First Order Upwind
H_2	First Order Upwind
CH_4	First Order Upwind
Energy	First Order Upwind

Finally, the very last step is to define the Under-Relaxation Factor (URF), they are not constant during calculations, but needs to be changed along with the evolution of the simulation. Because of the solution is not an analytical solution, but a numerical solution obtained after iterative methods, it needs to be stable enough and converge at a point so that the value is correct and close enough to reality. However, in iterative methods, the solution of an iteration depends on the previous iteration, this creates residuals that can become larger with the ongoing simulation. Therefore, sometimes this convergence is almost impossible if measures are not taken, in this case, finding a suitable URF is a good way to ensure stability and to find the desired solution. URF will limit the amount of change that can happen at each consecutive iteration (figure 11), and as a consequence, if the URF value is smaller means that this amount is smaller, enhancing the solution convergence. Otherwise, the explained residuals can skyrocket as shown in figure 12. Nevertheless, the computational cost and time must be taken into account as they will increase considerably with the reduction of URF [38,39]. An equilibrium between solution convergence and calculation time must be found.

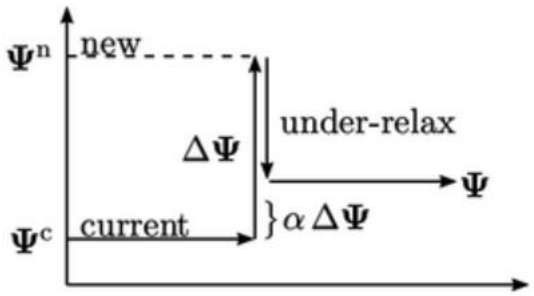

Figure 11: Graphic illustration of Under-Relaxation Factor [75]

From Figure 11: Ψ represents a cell in a solution step and its value shifts from Ψ^c to Ψ^n, URF is the α that limits the change $\Delta\Psi = \Psi^n - \Psi^c$. This α varies between 0 and 1. From figure 12, see how the residuals starts soaring rapidly after 7000 iterations, and then becomes mitigated by changing the URF to a smaller value. In this project, the values used are: 0.15 at the commencement, 0.1 after 8500 iterations, 0.07 after 9000 iterations, 0.03 after 11000 iterations approximately and finally 0.01 is used.

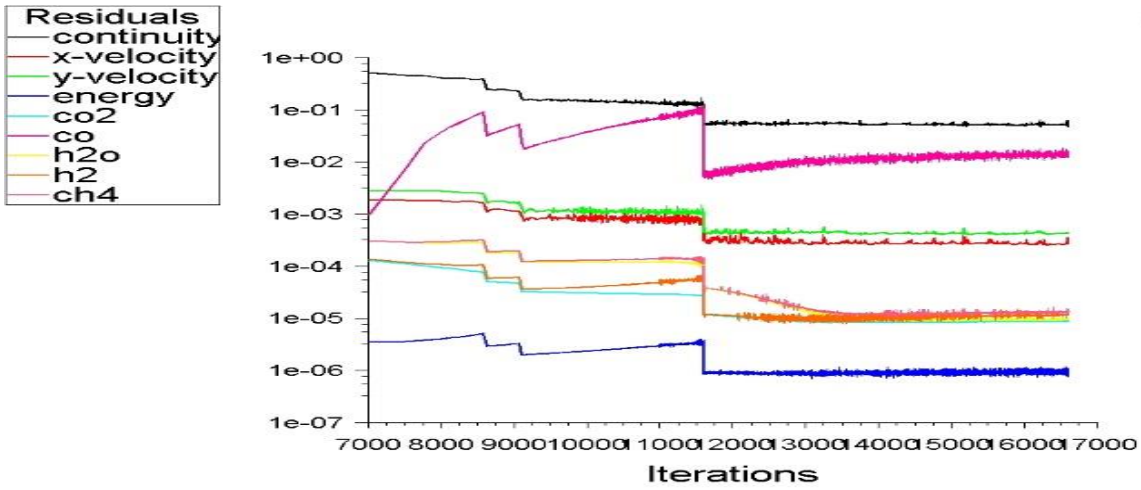

Figure 12: Residuals for the simulation of 'ADDmeth'. See how residuals drops immediately after reducing URF values.

3.2 USER DEFINED MEMORY

UDM (User Defined Memory) is the archive that will be loaded into ansys Fluent as a C code to read and work with the kinetic model (please see appendix). The first part will be used to define all necessary parameters such as enthalpy for different species. This second part is used to define and assign parameters such as temperature, pressure, or mole fraction to their corresponding function. The next part is to define the pressure for the species, to calculate the pressure, the ideal gas law, *pv=nrt,* as well as mole fraction formula have been considered (third part). The following part is to define the constants K for the kinetic model, these formulas are the same that can be found in table 7, equations 9 and 10 (fourth part).

Now that all parameters have been set, the kinetic model can be written and read: R_1_denomi stands for the denominator of r1 showed in equation 5; R_1a is the first part of r1 in the numerator; R_1b is the second part of r1 in the numerator; R_1c is the third part of r1 in the numerator and finally, R_1_1 is the combination of these 4 parts and together behaves as equation 5 in ansys FLUENT. Analogously, R_2_denomi, R_2a and R_2_2 works the same way but for equation 6.

In reality, whilst the reaction is ongoing, the quantity of catalyst that is adhered to the reacting substance is limited, this makes the reaction rate of each substance limited to a value (eq.20) plus the fact that the catalyst is porous itself, creates the pore diffusion effect, that can be provided by an analytical solution of the reaction-diffusion differential equation based on Thiele moduli or assumed as a fixed reaction rate.

$$\xi = r * \beta \qquad (20)$$

Where ξ is the actual reaction rate, r is the initial reaction rate, β an effectiveness factor given by Thiele moduli. Thiele reasoned that the catalyst would react only superficially, as the diffusion forces would interact just with the surface if the particle were large enough [18]. In other words, larger particles tend to have larger pore diffusion resistance, this resistance depends on gasification temperature, gasification agent and particle size, hence it is important to use the proper expression to express

pore diffusion. However, if the Thiele Modulus values is <0.4, this pore diffusion resistance can be neglected, on the other hand, if this value is >3, it means that the reaction rate is controlled by pore diffusion [45]. In this project, based on previous experience, different effectiveness factor of $\beta = 0.5, 0.8, 0.09$ will be used so the kinetic models will be adapted to the phseudohomogeneous reactor. In this way, R_1_1 will be limited to $\xi =$ 0.0005/0.0008/0.0003 as it is an exothermic reaction, meanwhile R_2_2 will be limited to $\xi =$ -0.0005/-0.0008/-0.0003 as it is an endothermic reaction. This is the second scenario, the geometry will still be fixed according to equations 17 and 18, and the heat transfer coefficient will be fixed to 3.176 (fifth part).

To close the loop, R1 and R2 will be combined to obtain ri, which represents the general reaction rate (sixth part). Utimately, source terms of the species need to be defined (seventh part).

Once this all is done, the simulation will take place. After obtaining the results, it will be compared to a simulation with a sparser mesh, with 8364 cells (basic cell size: 0.8), to a denser mesh, with 20852 cells (basic cell size: 1.3) and to another mesh with 52562 cells (basic size: 0.5). This is known as independent test.

3.3 GEOMETRY CHANGES

For the third and last scenario, the basic cell size of 0.8 will be the chosen to run the calculations, as 1 and 1.3 have not shown a reasonable convergence result, and 0.5 is computationally excessively costly. It is here where the geometry of the reactor will be modified, the conical curves that are shown in figure 4 will be modified, the x-label will be extended to 160 cm and the rest will remain constant. The heat transfer coefficient will be fixed to 3.176, and reaction rate will be 0.0005.

The same equation utilized in the equation 17 (curve 3) also applies in this new curve as it is an exponential equation, in this sense, the Δy that is obtained by subtracting each value y to its previous value y (table 23), will be multiplied by *0.3, *0.7, *1.3 and *1.7 respectively to tighten or broaden the outlet size of the reactor, giving place to new curves (figure 13) and accordingly, new parametrizing equations (Table 24).

Table 23: Δy used to obtain the curves

Δy	Δy*0,7	Δy*0,3	Δy*1,3	Δy*1,7
0.60563738	0.42394617	0.18169121	0.7873286	1.02958355
0.74162957	0.5191407	0.22248887	0.96411845	1.26077028
0.78237372	0.5476616	0.23471212	1.01708584	1.33003533
0.82513145	0.57759202	0.24753944	1.07267089	1.40272347
1.09085066	0.76359547	0.3272552	1.41810586	1.85444613
1.17717778	0.82402445	0.35315333	1.53033111	2.00120222
1.42294985	0.9960649	0.42688496	1.84983481	2.41901475
1.56776452	1.09743517	0.47032936	2.03809388	2.66519969
1.82391937	1.27674356	0.54717581	2.37109518	3.10066293
1.9626559	1.37385913	0.58879677	2.55145267	3.33651503

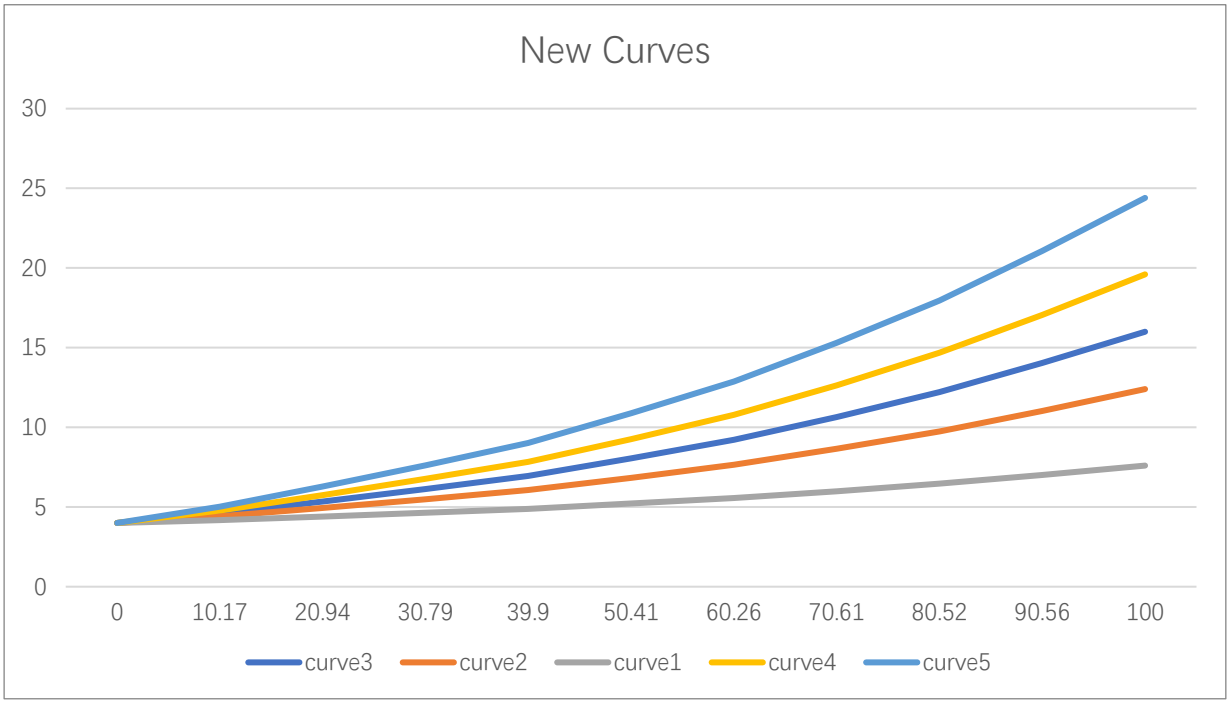

Figure 13: All new curves used for the third scenario

Table 24: New parametrizing equations of the curves that will be loaded into Catia V5.

*0.3	$y = 4 * \exp(0.006419 * x * 100)$	(24)	(curve 1)	Ø5.6mm
*0.7	$y = 4 * \exp(0.0113142 * x * 100)$	(22)	(curve 2)	Ø10.4mm
	$y = 4 * \exp(0.0139 * x * 100)$	(17)	(curve 3)	Ø16.0mm
*1.3	$y = 4 * \exp(0.0158928 * x * 100)$	(21)	(curve 4)	Ø17.6mm
*1.7	$y = 4 * \exp(0.018083 * x * 100)$	(23)	(curve 5)	Ø22.4mm

Finally, the last step is to repeat the explained methodology for all 5 new curves and then compare the results.

4. RESULTS

4.1 FIRST SCENARIO

The first scenario only varies the heat transfer coefficient whereas 3.176 W/mK is represented by the black curve, 1.65 W/mK is represented by the red curve and 2.56 W/mK is represented by the green curve, the results of this variation are shown:

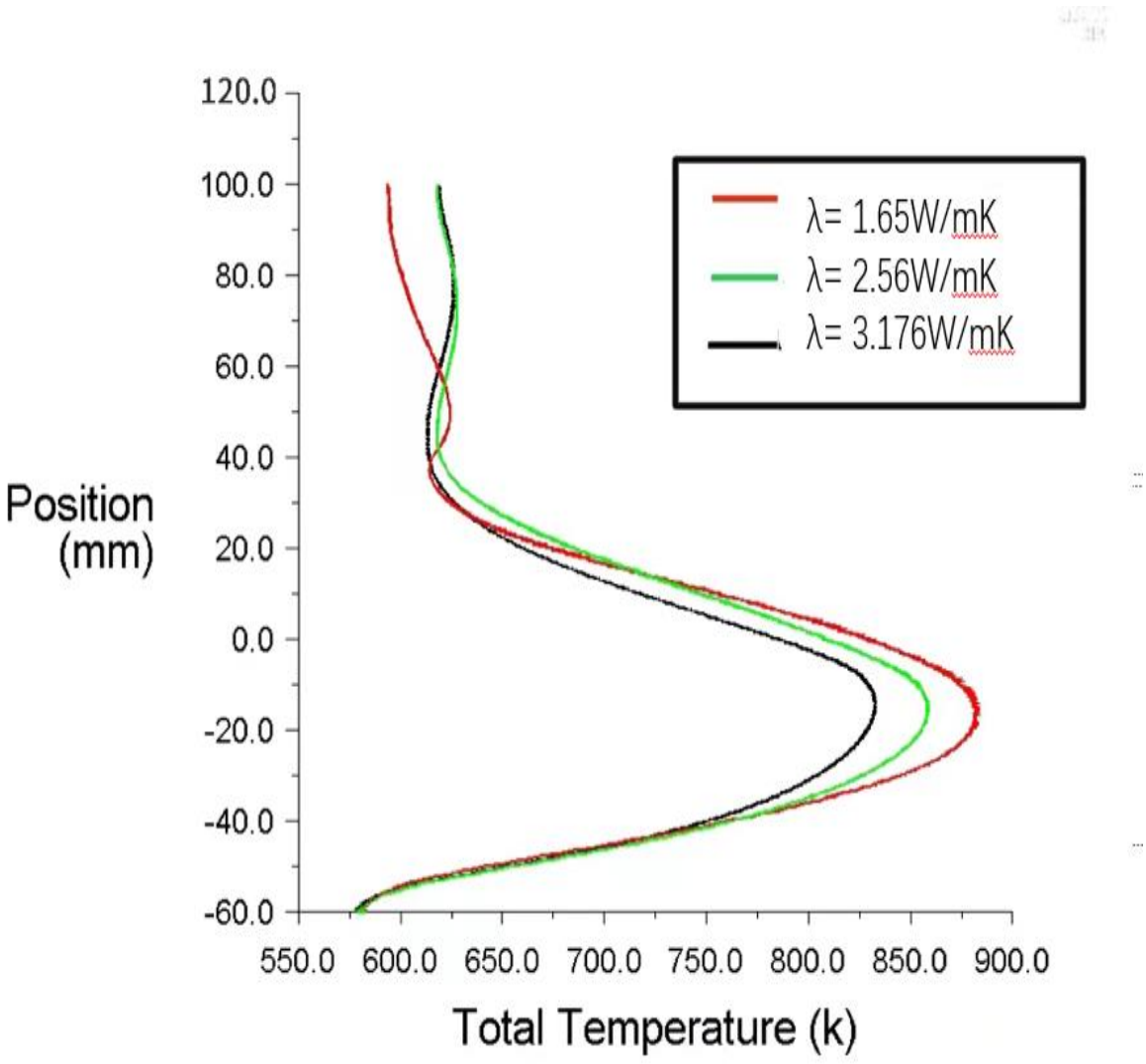

Figure 14: Results of variating the heat transfer coefficient.

Changing the heat transfer coefficient does not affect much the wavelength of the curve, therefore the reactions are still produced at almost the same location in the reactor. However, the curve shows that the maximum temperature has an inverse relationship to this coefficient, this is mainly because the fact that heat transfer coefficient has a direct relationship to the heat dissipation of the reactor, so if this is lower, the heat dissipation will be more difficult resulting in a higher peak temperature.

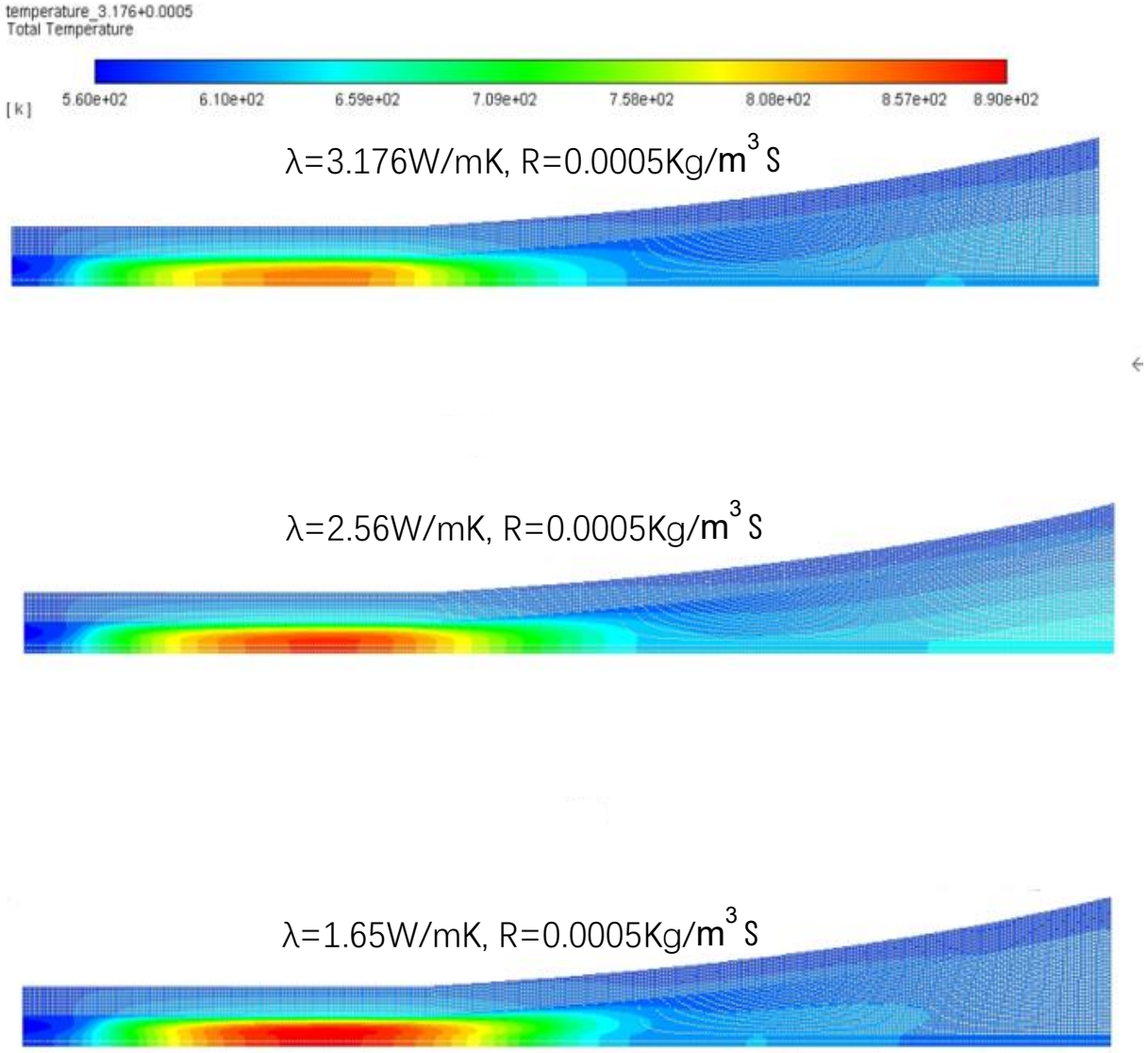

Figure 15: Heat maps of using different heat transfer coefficients.

Figure 15 makes a comparison of the different heat maps, it shows how using smaller heat transfer coefficients indeed increases the peak temperature, which is represented by a more intense red in the graphic.

4.2 SECOND SCENARIO

The second scenario varies the reaction rate, black curve still corresponds to 0.0005, the red curve represents 0.0008 and 0.00009 is presented as the green curve. It is easy to see how this affects the curves a lot as the red curve has a much higher temperature peak, but broads a smaller area, with a tighter V-shape. However, the black curve, with still high temperature, covers a wider range in the reactor within more favorable heat, and its V-shape arranges almost half reactor. Finally, the green curve seems to have the lowest maximum temperature, that is produced in the

second part of the reactor, however, this temperature might be too low, which is not ideal as it may slow the reaction rate and efficiency of the entire process (Figure 16). This indicates that the higher the reaction rate, the higher the peak temperature will be and the location where this peak is produced tends to move towards the end of the reactor as the reaction rate is reduced. All these facts shows how changing the reaction rate is probably a reasonable way to accomplish a wider area of high working temperature. Results of solutions will be presented as graphics of distribution of temperature, mole fraction of CH_4 and reaction rate profile of CH_4, the same will be done with hydrogen. This will be applied to each reaction rate.

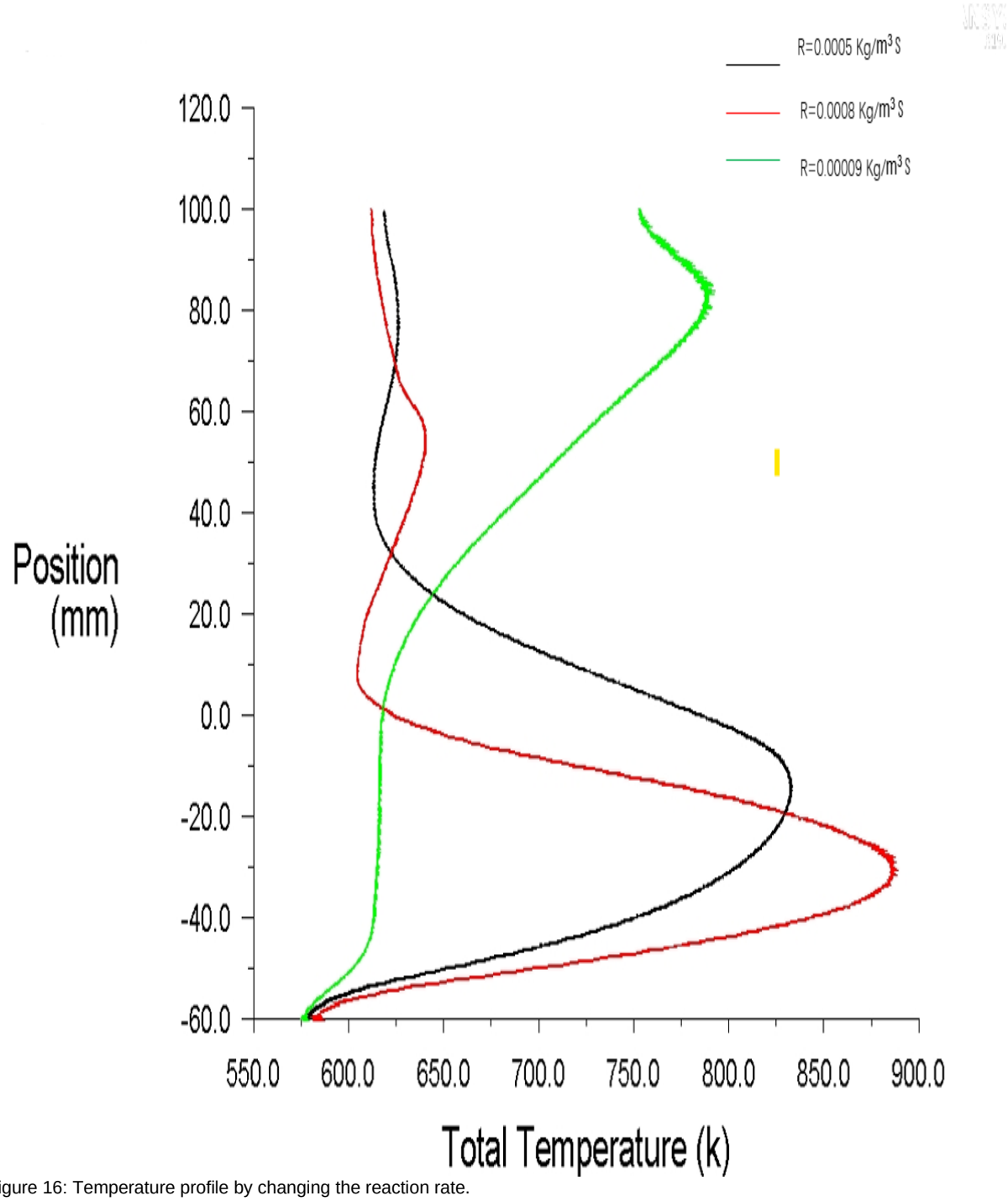

Figure 16: Temperature profile by changing the reaction rate.

For reaction rate as 0.0005, results are displayed in figures 17, 18, 19, 20 and 21.

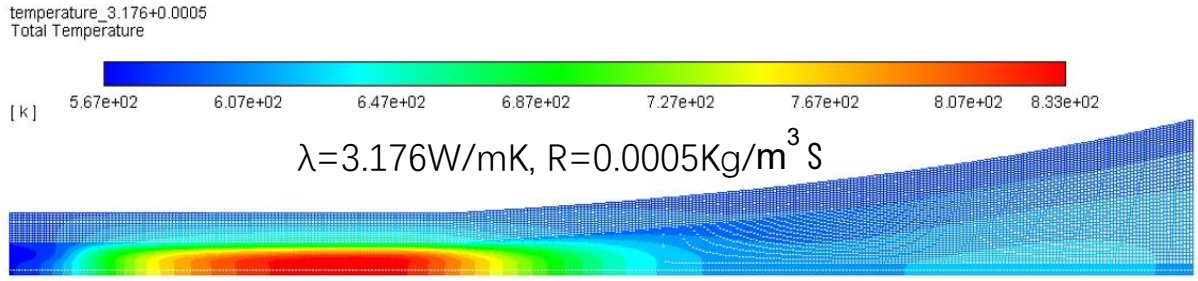

Figure 17: Temperature for reaction rate of 0.0005

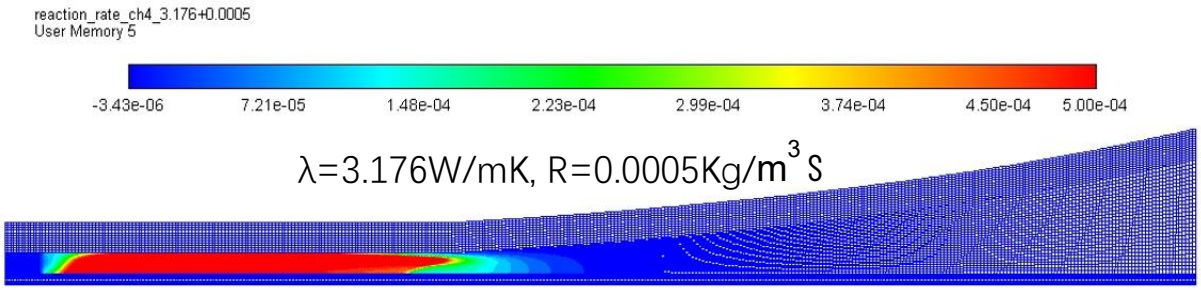

Figure 18: Reaction rate profile of CH4 for reaction rate of 0.0005

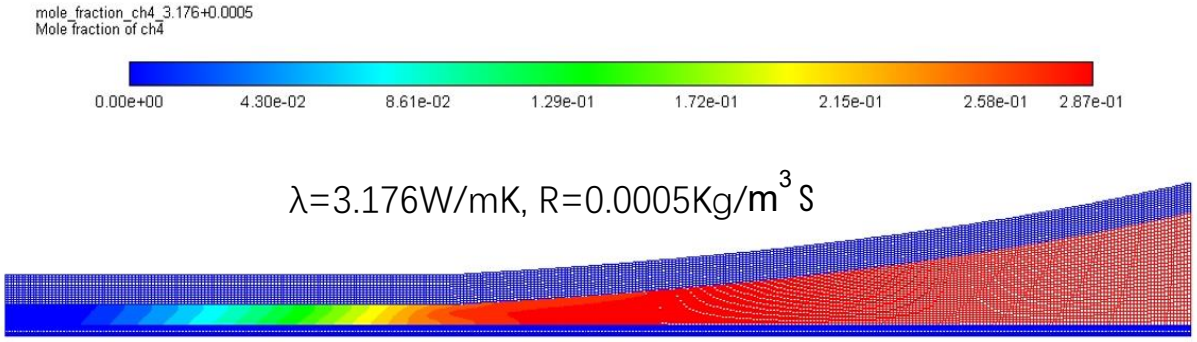

Figure 19: Mole fraction of CH4 for reaction rate of 0.0005

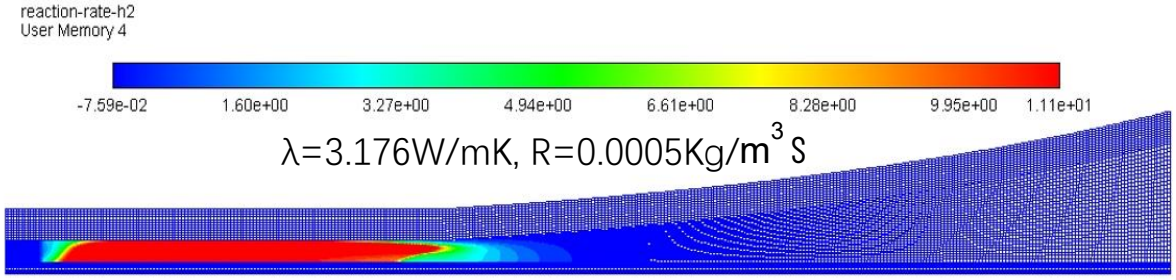

Figure 20: Reaction rate profile of H2 for reaction rate of 0.0005

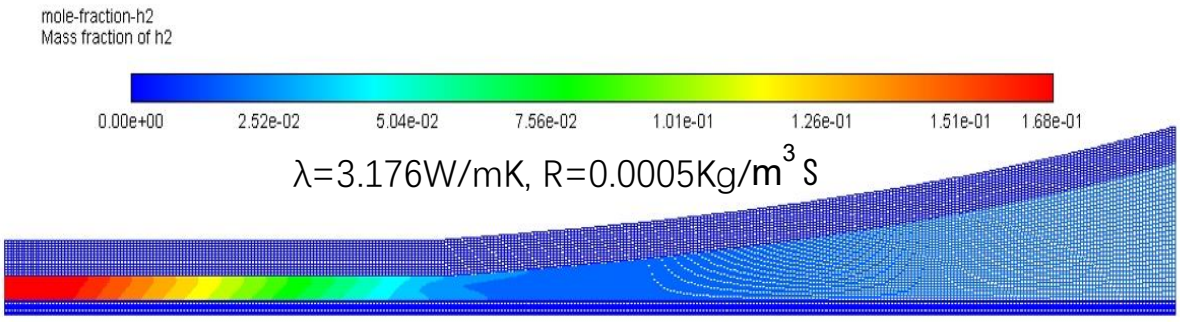

Figure 21: Mole fraction of H2 for reaction rate of 0.0005

For reaction rate as 0.0008, results are displayed in figures 22,23,24,25 and 26.

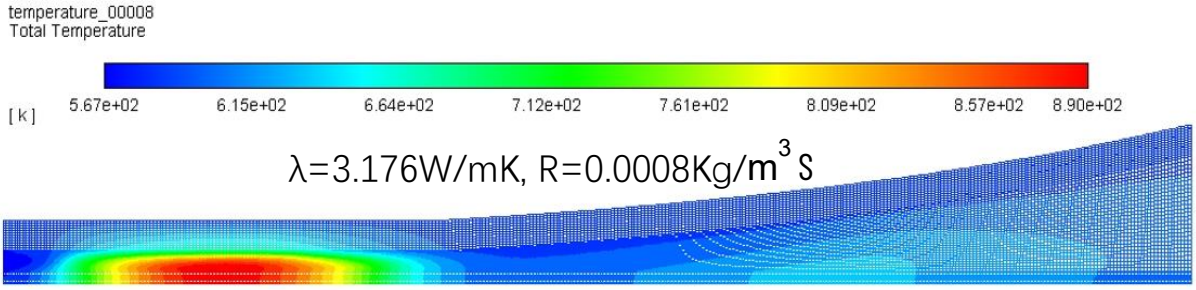

Figure 22: Temperature for reaction rate of 0.0008

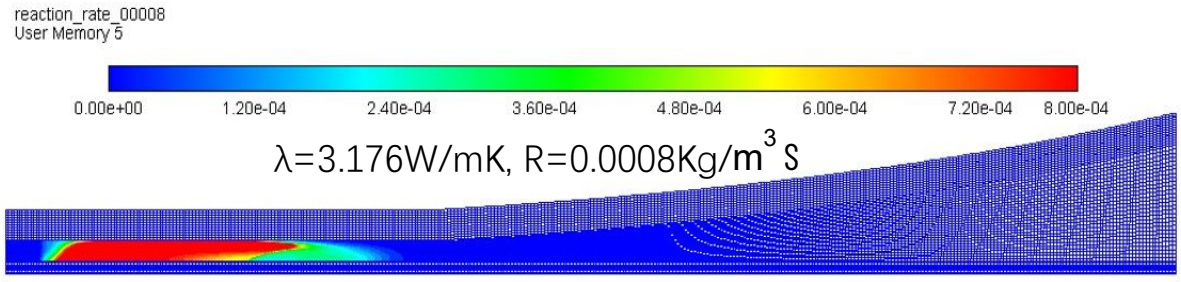

Figure 23: Reaction rate profile of CH4 for reaction rate of 0.0008

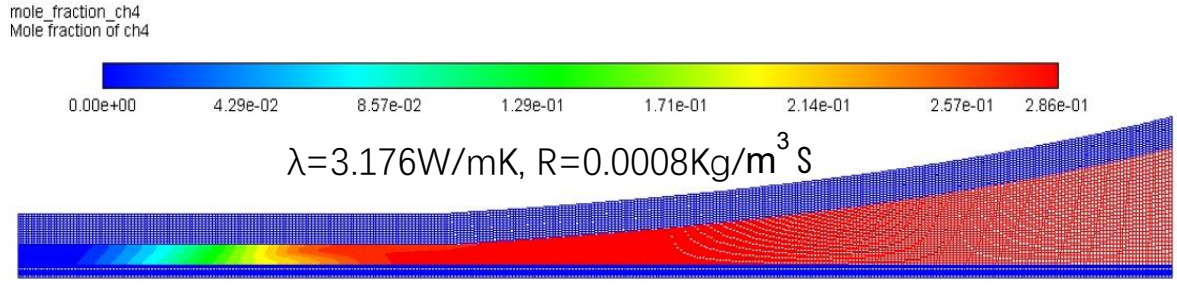

Figure 24: Mole fraction of CH4 for reaction rate of 0.0008

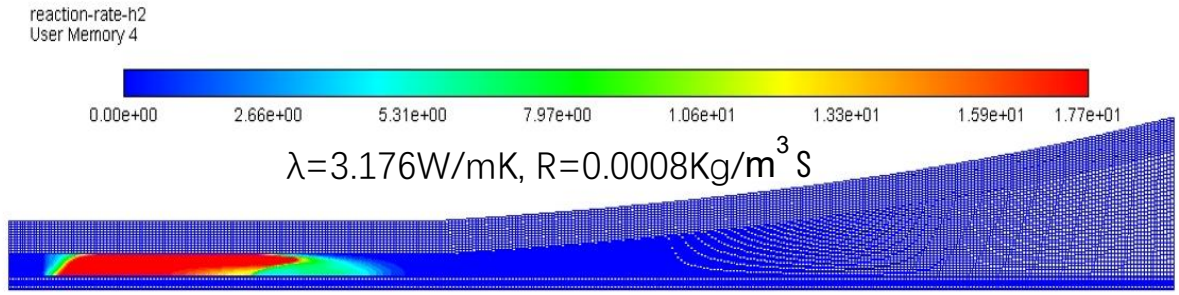

Figure 25: Reaction rate profile of H2 for reaction rate of 0.0008

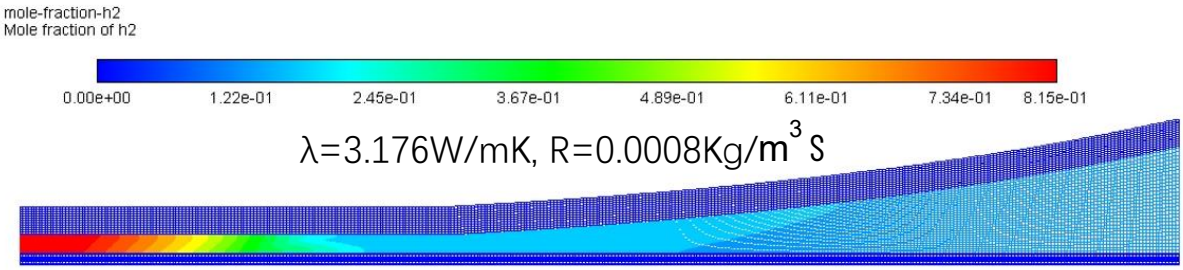

Figure 26: Mole fraction of H2 for reaction rate of 0.0008

For reaction rate as 0.00009, results are displayed in figures 27,28,29,30 and 31.

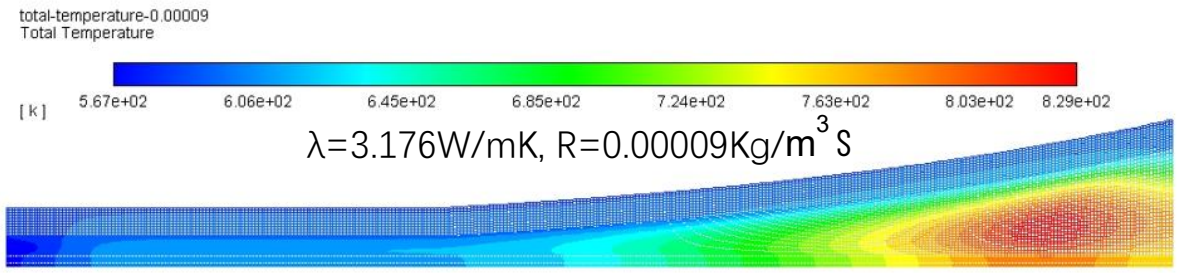

Figure 27: heat map for reaction rate of 0.00009

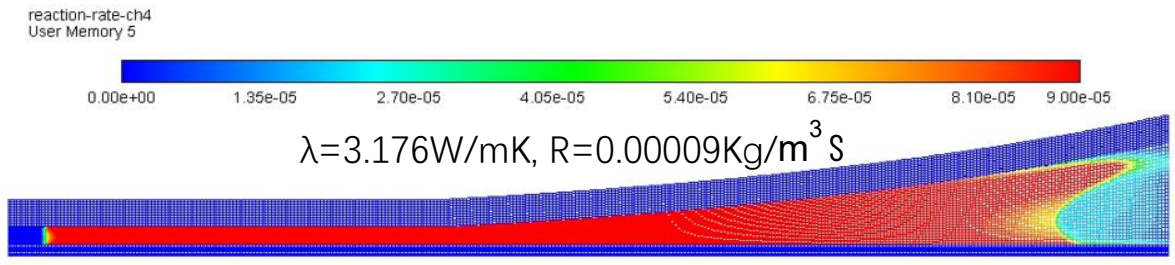

Figure 28: Reaction map for reaction rate of 0.00009

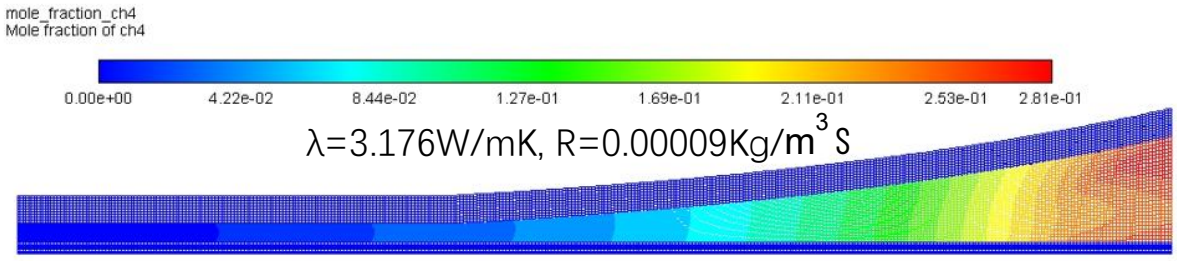

Figure 29: Mole fraction of ch4 for reaction rate of 0.00009

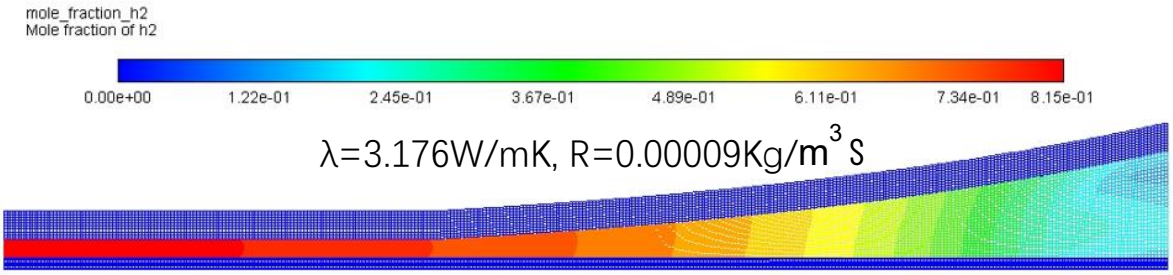

Figure 30: Mole fraction of h2 for reaction rate of 0.00009

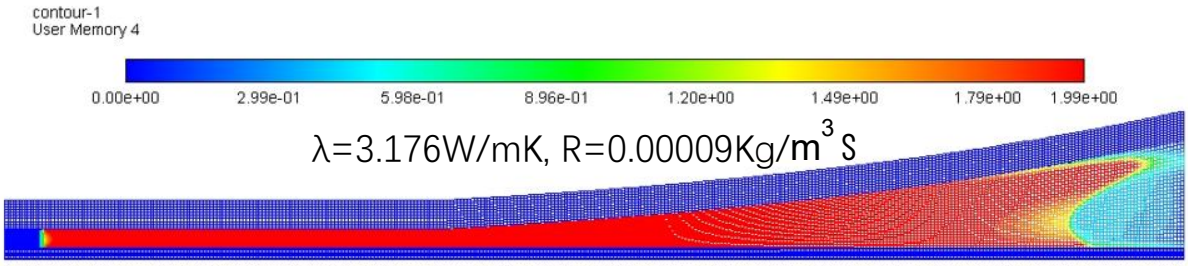

Figure 31: Reaction map for reaction rate of 0.00009

The area where the maximum temperature is produced coincides with the zone where the maximum reaction of both hydrogen and methane happens. On the other hand, the mole fraction of hydrogen is maximum at the beginning of the reactor and decreases with the evolution of the reaction. The opposite happens for the methane, is null at the beginning but increasing whilst the reaction occurs. Moreover, it is shown that the lower the reaction rate is, the lower is the peak temperature, the profile of the reaction is more extended, and the reacting temperature is also distributed more evenly, although leaning to the end of the reactor. Considering the pore diffusion effect, if the reaction rate is lower means that the effectiveness factor is also lower according to equation 20, and hence each catalyst reacts less. In this sense, more quantity of catalyst will be needed to react properly, and this is only found in the wider zones of the reactor, where more reactant is available. This is the reason why, by limiting the reaction rate, high temperatures will be produced towards the end of the reactor, and also, a more even heat distribution map is achieved.

4.3 THIRD SCENARIO

Into the third scenario, in which the heat transfer coefficient is fixed to 3.176 W/m-k and reaction rate is set 0.0005, different geometries have been simulated and the results are displayed:

After simulating all 5 new curves according to equations 17, 21, 22, 23, 24, figure 32 was obtained in which illustrates how the changing geometry affects the evolution of temperature depending on axis z (mm):

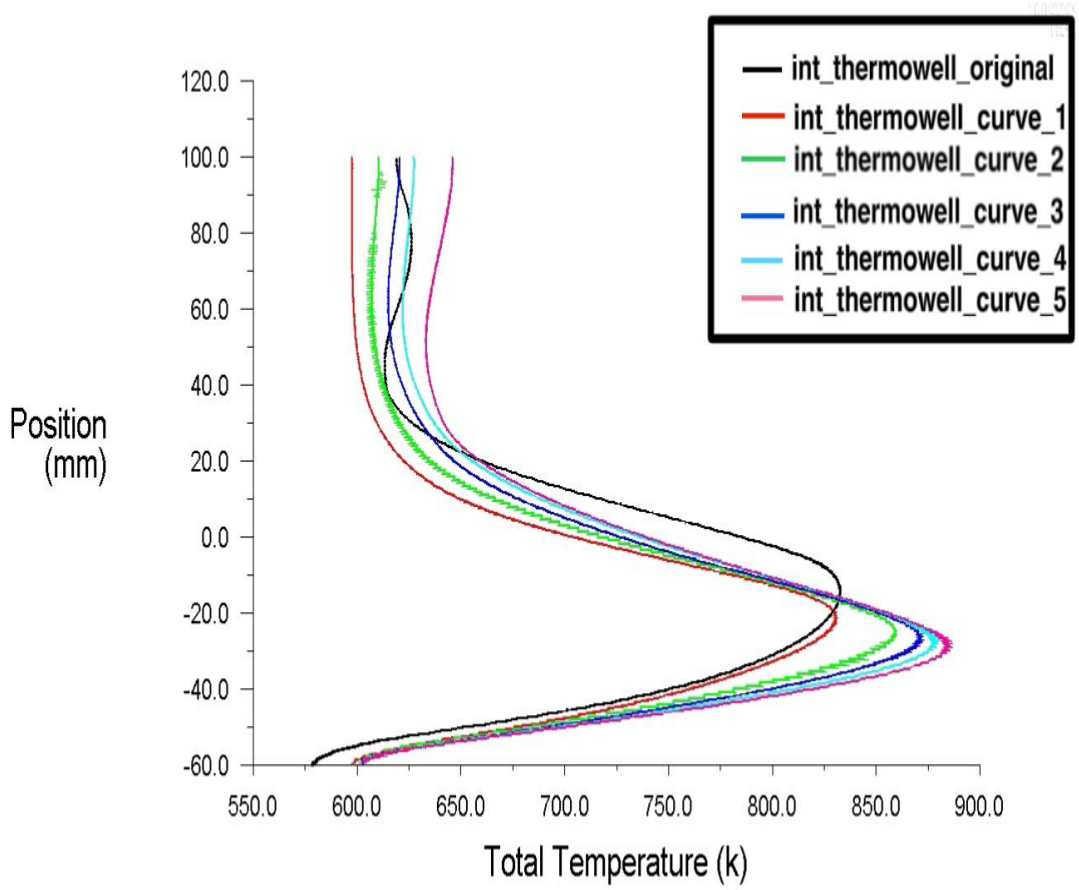

Figure 32: Temperature profile of different geometries for the reactor.

In this graphic, the maximum peak temperature is set by the pink curve with 890K, which has an outlet diameter of 22.4mm (equation 23), it is followed by the cyan curve with 883k and an outlet diameter of 17.6mm (equation 21), then comes the dark blue curve, its peak temperature is 876K and the outlet diameter is16mm (equation 17). After this curve, the green curve has a maximum temperature of 863K, and an outlet diameter of 10.4mm (equation 22), finally the red curve has the lowest peak temperature with only 834K and also the smallest outlet diameter of 5.6mm (equation 24). The black curve corresponds to the original curve, it has a wider outlet (16mm) but its outlet temperature the lowest with only 833k. Note how the peak temperatures are still produced at -30mm of the reactor which is 30mm if the origin of coordinates is set to 0. It then falls quickly and stabilizes producing a V-shape

temperature profile meaning that the reaction has been produced concentratedly in this position. It seems therefore that changing geometry does not guarantee a better high temperature distribution and other factors need to be studied and considered whilst attempting so. However, after changing the geometry, where now the entire curve follows the conic shape equation since the beginning to the ending of the reactor (since -60mm to 100mm instead of being first consistently horizontal from -60mm to 0mm and then conic from 0mm to 100mm), a displacement in the location where the highest temperature is produced has occurred, this is mainly due to the change of the geometry, if the entire curve is conic, the reacting zone is progressively bigger (instead of consistent in the first 60mm) therefore there will be more space and reactant to react, achieving higher temperatures in earlier stages of the reactor.

Figure 33 shows the yield of H_2. Figure 34 shows the yield of CH_4, see how the hydrogen yield gets smaller with higher outlet diameters and therefore the difference to experimental data is bigger. The vice versa occurs for CH_4.

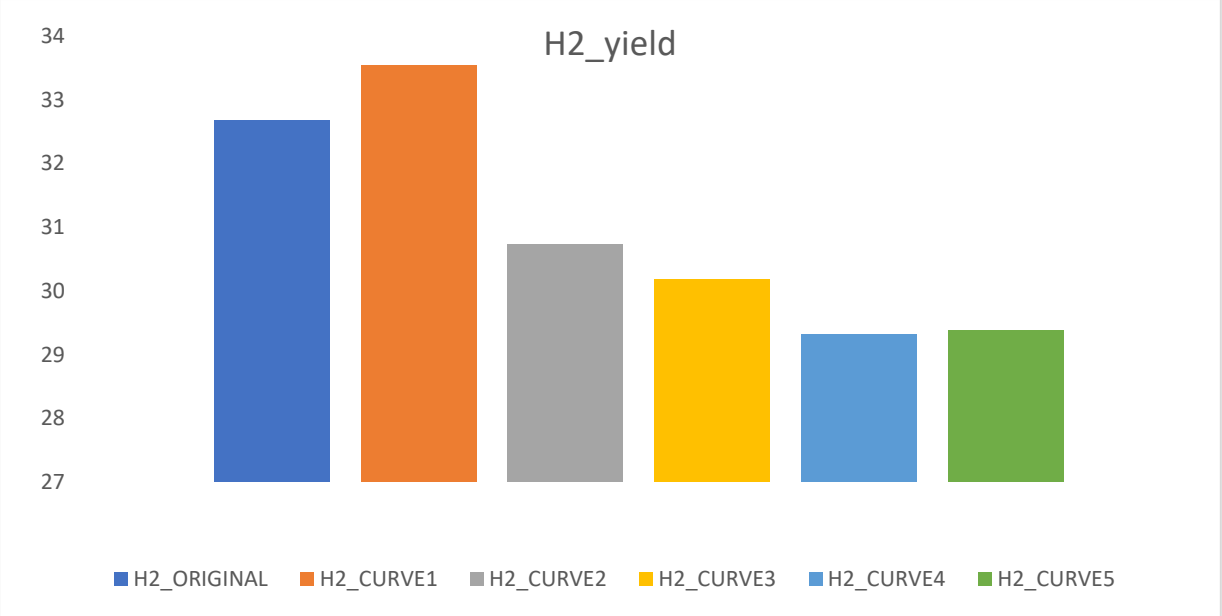

Figure 33: H_2 yield of the different geometries

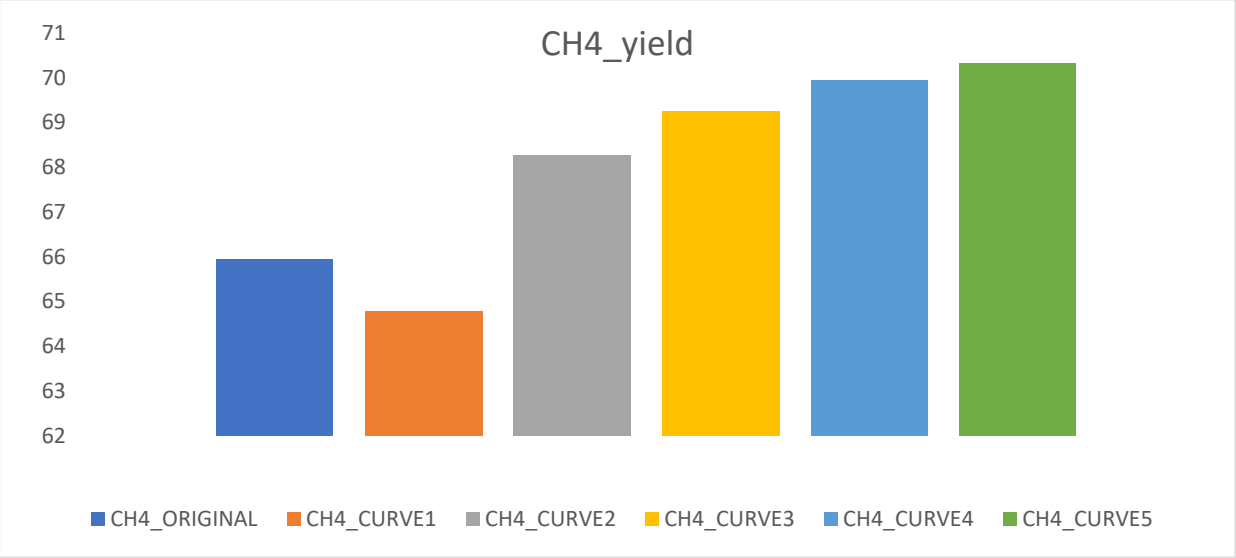

Figure 34:CH_4 yield of the different geometries

Figures 35, 36, 37, 38, 39, and 40 shows the hydrogen and methane yield comparing the simulated result to the experimental result, as the outlet diameter gets bigger, the difference between them also increases, however they do it in two completely opposite directions: simulated hydrogen yield is each time smaller than experimental hydrogen yield but the simulated methane yield is each time higher than experimental methane yield.

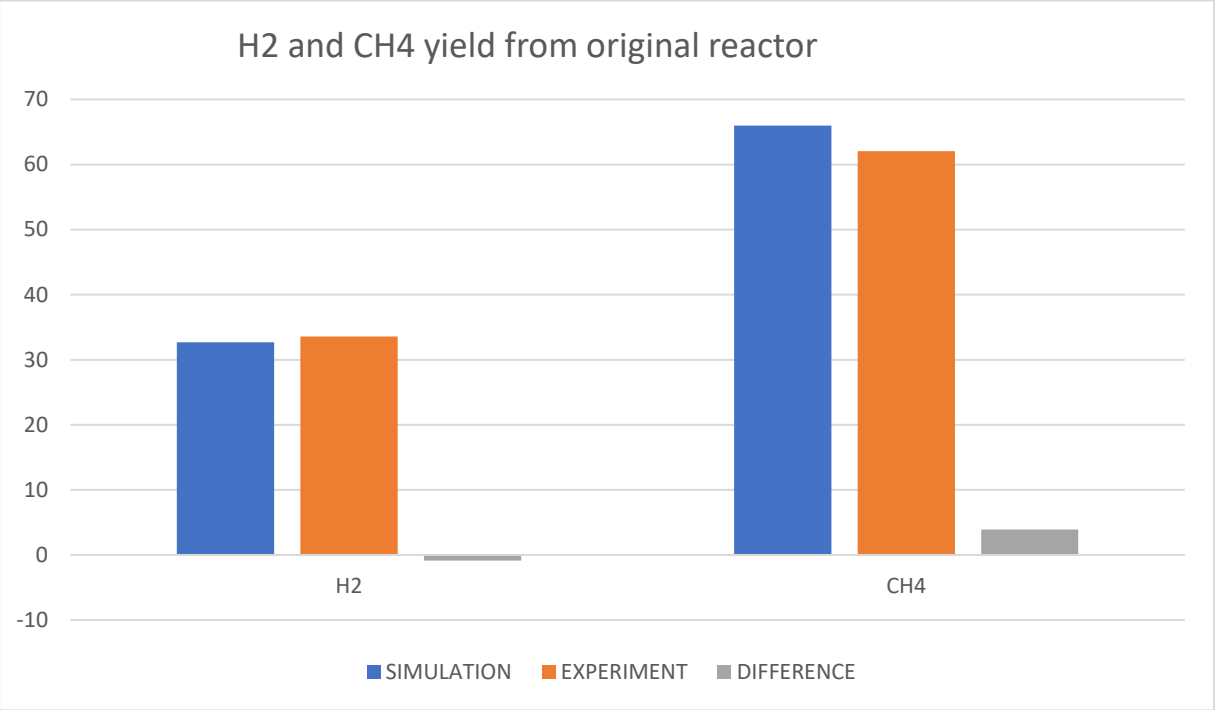

Figure 35: comparison of hydrogen and methane yield for the original reactor.

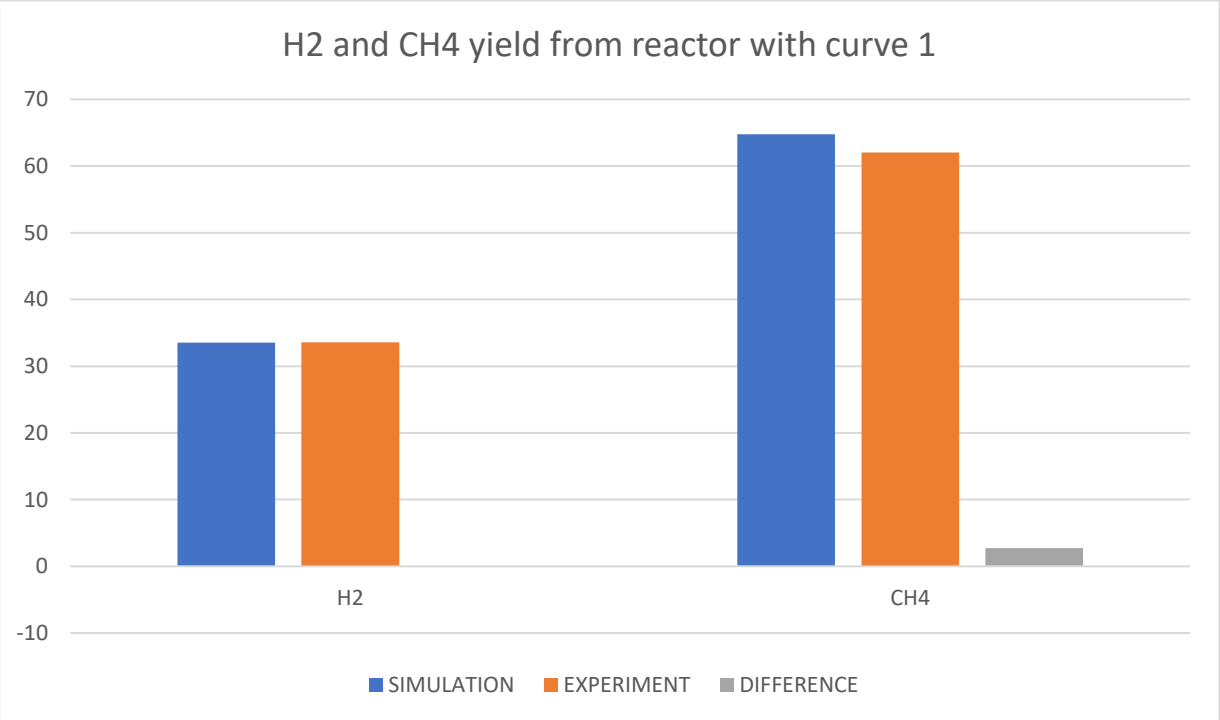

Figure 36: comparison of hydrogen and methane yield for the reactor with curve 1.

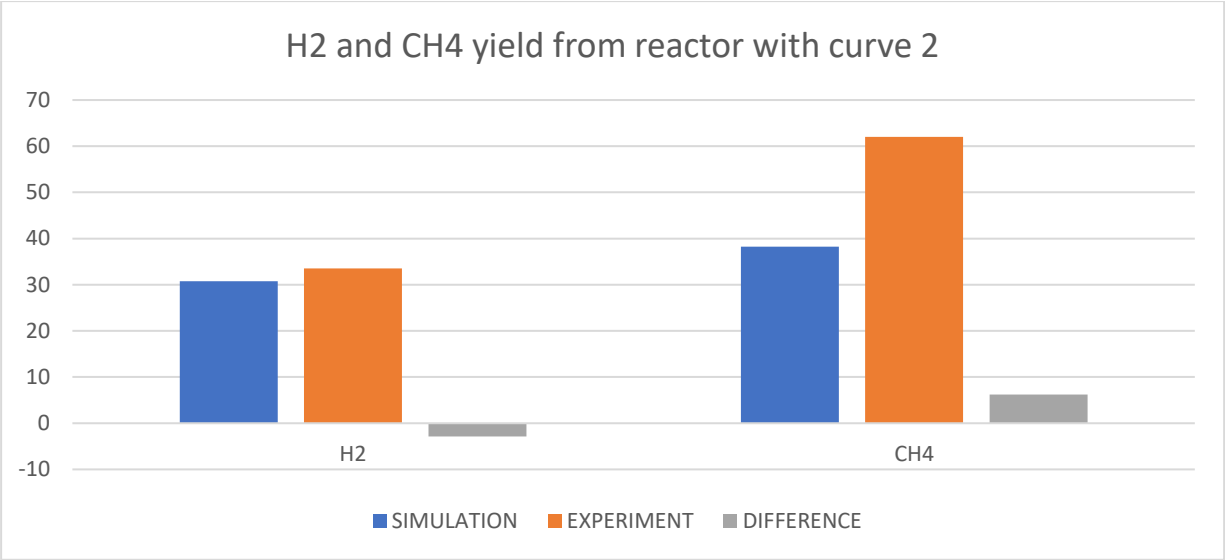

Figure 37: comparison of hydrogen and methane yield for the reactor with curve 2.

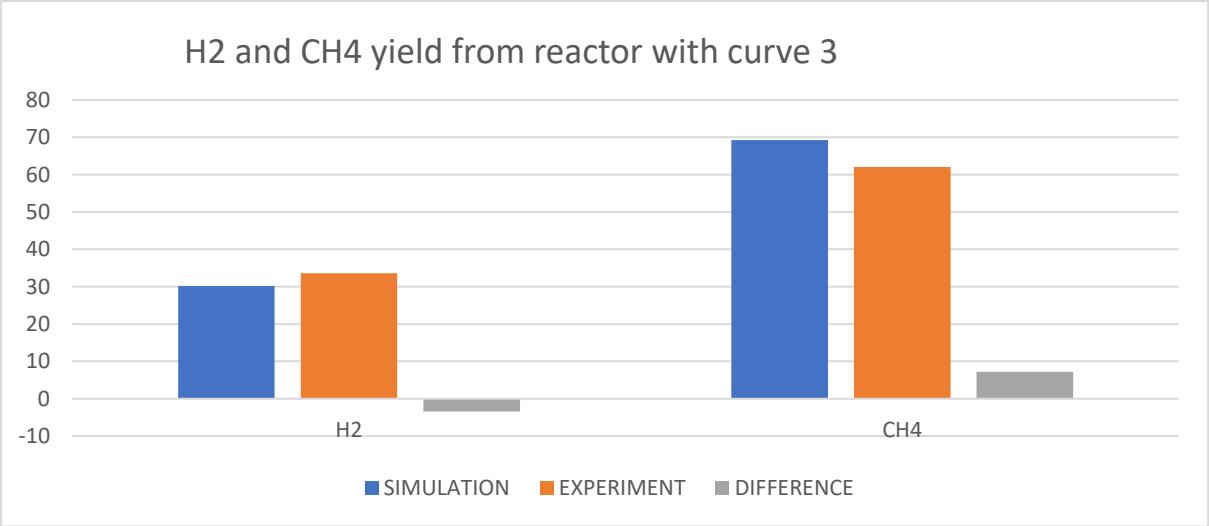

Figure 38: comparison of hydrogen and methane yield for the reactor with curve 3.

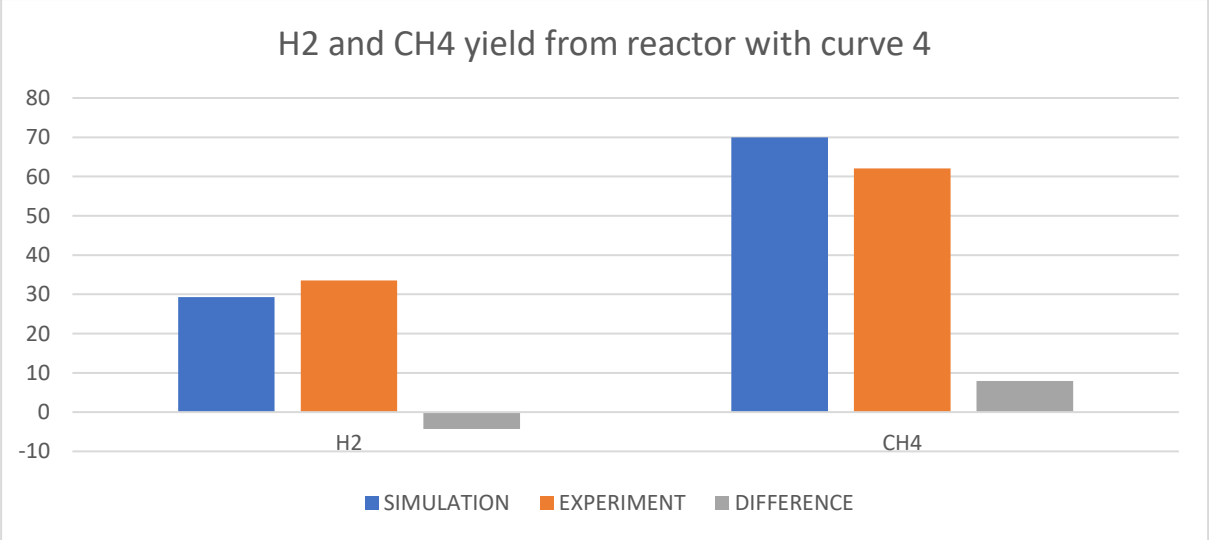

Figure 39: comparison of hydrogen and methane yield for the reactor with curve 4.

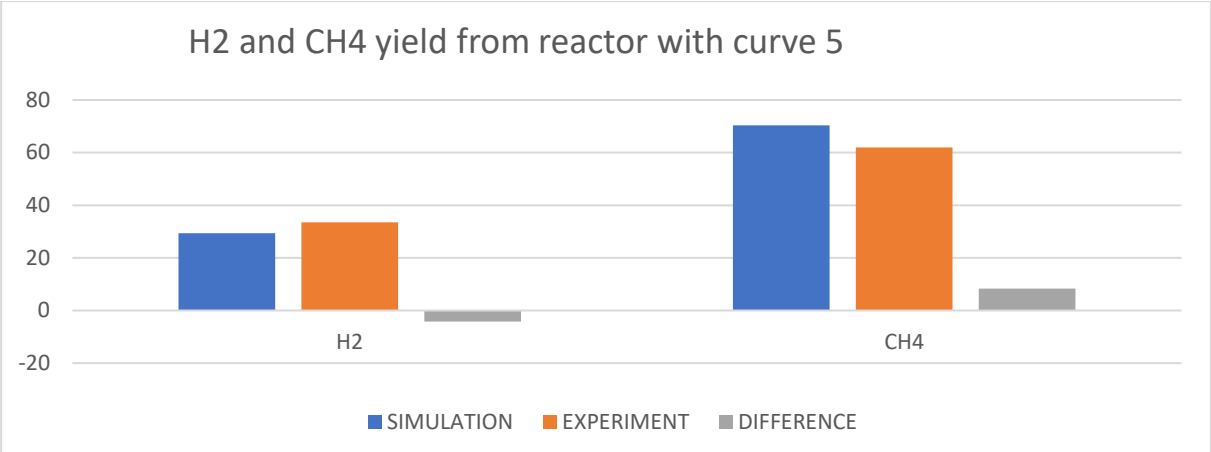

Figure 40: comparison of hydrogen and methane yield for the reactor with curve 5.

Finally, a comparison of the heat map of the different reactors will be made, this is shown in figure 41. Something similar to the first scenario happens, in this case, even every parameter have remained the same, the wider outlet diameter, and therefore the wider reacting area, has contributed to a higher temperature, and this can be effectively seen in the mentioned figure, which is represented by red zones that are getting more intense each time.

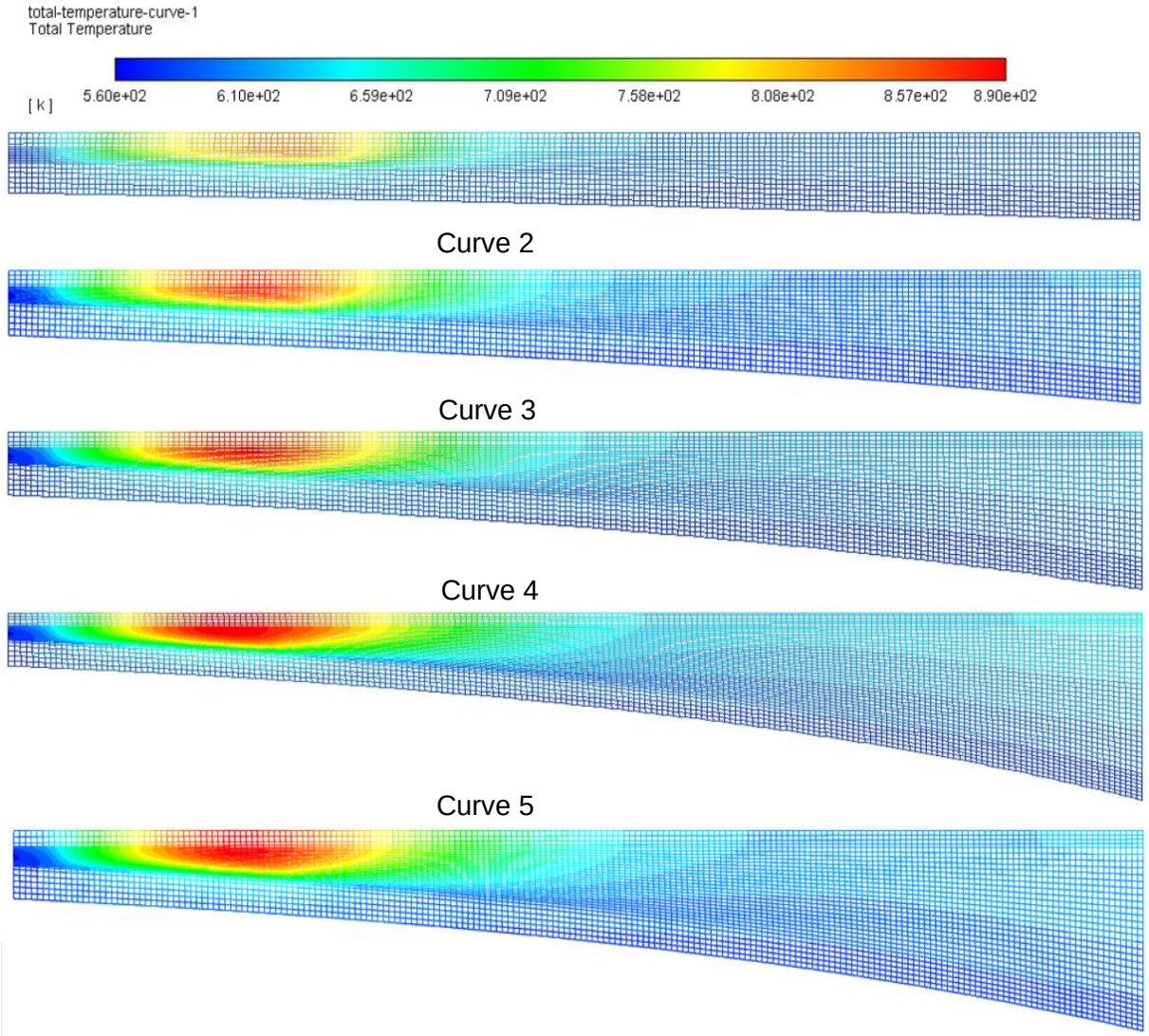

Figure 41: Heat map of the different reactor curves.

5.CONCLUSION

After a thorough examination of the whole issue. It seems that changing the reaction rate is the best way to achieve a more controllable temperature and reacting profile, however, in this case these values have been an assumed fixed value that are used for the discover of a pattern. On the other hand, changing the heat transfer only varies the absolute value of the peak temperature, in this work they have also been assumed to observe a patter therefore not suitable for an exact conclusion. Finally, with the change to the geometry of the reactor, an important displacement whereas the highest temperature is produced has be discovered, meaning that they have a direct relationship, this could be of great help trying to settle future paths to the enhanced control of the temperature. It also seems to increase the production of methane when the outlet diameter increases. Nevertheless, in the process of its calculation, the heat transfer and reaction rate used are also assumed values that are not precise when it comes to realizing the actual dual-function reactor. In conclusion, the 2 most important parameters: heat transfer coefficient and reaction rate coefficient must be calculated reasonably, precisely and adequately before trying to reach any change of the geometry. This work has given some ideas of how the reactor would perform in response to the thermodynamic, kinetic and geometric changes made, but they are suppositions, and the actual performance is still an unknown.

6.REFERENCE

[1] G.Gourisankaran, Stanley S. Reynolds, M.Samano. “Intermittency and the Value of Renewable Energy”. Journal of Political Economy.2016.124. (4).1187-1234.

[2] OBERHOFER, Andreas; MEISEN, Peter. Energy storage technologies & their role in renewable integration. *Global Energy Network Institute*, 2012, vol. 1.

[3] GÖTZ, Manuel, et al. Renewable Power-to-Gas: A technological and economic review. *Renewable energy*, 2016, vol. 85, p. 1371-1390.

[4] WULF, Christina; LINßEN, Jochen; ZAPP, Petra. Review of power-to-gas projects in Europe. *Energy Procedia*, 2018, vol. 155, p. 367-378.

[5] CLEGG, Stephen; MANCARELLA, Pierluigi. Storing renewables in the gas network: modelling of power‐to‐gas seasonal storage flexibility in low‐carbon power systems. *IET Generation, Transmission & Distribution*, 2016, vol. 10, no 3, p. 566-575.

[6] LEWANDOWSKA-BERNAT, Anna; DESIDERI, Umberto. Opportunities of power-to-gas technology in different energy systems architectures. *Applied energy*, 2018, vol. 228, p. 57-67.

[7] MEBRAHTU, Chalachew, et al. CO2 methanation: principles and challenges. En *Studies in surface science and catalysis*. Elsevier, 2019. p. 85-103.

[8] DIAS, Yan Resing; PEREZ-LOPEZ, Oscar W. CO2 methanation over Ni-Al LDH-derived catalyst with variable Ni/Al ratio. *Journal of CO2 Utilization*, 2023, vol. 68, p. 102381.

[9] Hauser, A.; Neubert, M.; Feldner, A.; Horn, A.; Grimm, F.; Karl, J. Design and Implementation of an Additively Manufactured Reactor Concept for the Catalytic Methanation. *Appl. Sci.* **2022**, *12*,9393.

[10] MOLINO, Antonio; CHIANESE, Simeone; MUSMARRA, Dino. Biomass gasification technology: The state of the art overview. *Journal of Energy Chemistry*, 2016, vol. 25, no 1, p. 10-25.

[11] KAN, Tao, et al. Production of gasoline and diesel from coal tar via its catalytic hydrogenation in serial fixed beds. *Energy & fuels*, 2012, vol. 26, no 6, p. 3604-3611.

[12] M. GÖtz, J. Lefebvre, F. Mo¨rs, A. McDaniel Koch, F. Graf, S. Bajohr, R. Reimert, T. Kolb, Renewable Energy 2016, 85, 1371–1390. DOI: https://doi.org/10.1016/ j.renene.2015.07.066

[13] RÖNSCH, Stefan, et al. Review on methanation–From fundamentals to current projects. *Fuel*, 2016, vol. 166, p. 276-296.

[14] NGUYEN, T. T. M.; WISSING, L.; SKJØTH-RASMUSSEN, M. S. High temperature methanation: Catalyst considerations. *Catalysis today*, 2013, vol. 215, p. 233-238.

[15] STANGELAND, Kristian, et al. CO2 methanation: the effect of catalysts and reaction conditions. *Energy Procedia*, 2017, vol. 105, p. 2022-2027.

[16] GAO, Jiajian, et al. A thermodynamic analysis of methanation reactions of carbon oxides for the production of synthetic natural gas. *RSC advances*, 2012, vol. 2, no 6, p. 2358-2368.

[17] MILLS, G. Alex; STEFFGEN, Fred W. Catalytic methanation. *Catalysis Reviews*, 1974, vol. 8, no 1, p. 159-210.

[18] SCHARL, Valentin, et al. Applying Reaction Kinetics to Pseudohomogeneous Methanation Modeling in Fixed‐Bed Reactors. *Chemical Engineering & Technology*, 2020, vol. 43, no 6, p. 1224-1233.

[19] GHAIB, Karim; NITZ, Korbinian; BEN‐FARES, Fatima‐Zahrae. Chemical methanation of CO2: a review. *ChemBioEng Reviews*, 2016, vol. 3, no 6, p. 266-275.

[20] RÖNSCH, Stefan, et al. Global reaction kinetics of CO and CO2 methanation for dynamic process modeling. *Chemical Engineering & Technology*, 2016, vol. 39, no 2, p. 208-218.

[21] KOPYSCINSKI, Jan, et al. Applying spatially resolved concentration and temperature measurements in a catalytic plate reactor for the kinetic study of CO methanation. *Journal of Catalysis*, 2010, vol. 271, no 2, p. 262-279.

[22] SCHLERETH, David; HINRICHSEN, Olaf. A fixed-bed reactor modeling study on the methanation of CO2. *Chemical Engineering Research and Design*, 2014, vol. 92, no 4, p. 702-712.

[23] XU, Jianguo; FROMENT, Gilbert F. Methane steam reforming, methanation and water‐gas shift: I. Intrinsic kinetics. *AIChE journal*, 1989, vol. 35, no 1, p. 88-96.

[24] KLOSE, J.; BAERNS, M. Kinetics of the methanation of carbon monoxide on an alumina-supported nickel catalyst. *Journal of Catalysis*, 1984, vol. 85, no 1, p. 105-116.

[25] KOSCHANY, Franz; SCHLERETH, David; HINRICHSEN, Olaf. On the kinetics of the methanation of carbon dioxide on coprecipitated NiAl (O) x. *Applied Catalysis B: Environmental*, 2016, vol. 181, p. 504-516.

[26] KOPYSCINSKI, Jan, et al. Applying spatially resolved concentration and temperature measurements in a catalytic plate reactor for the kinetic study of CO methanation. *Journal of Catalysis*, 2010, vol. 271, no 2, p. 262-279.

[27] ZHANG, Jie, et al. Kinetic investigation of carbon monoxide hydrogenation under realistic conditions of methanation of biomass derived syngas. *Fuel*, 2013, vol. 111, p. 845-854.

[28] ELNASHAIE, Said SEH. *Modelling, simulation and optimization of industrial fixed bed catalytic reactors*. CRC Press, 1994.

[29] ZAWAWI, Mohd Hafiz, et al. A review: Fundamentals of computational fluid dynamics (CFD). En *AIP conference proceedings*. AIP Publishing LLC, 2018. p. 020252.

[30] AL-BAALI, AG Abdul-Ghani, et al. Fundamentals of computational fluid dynamics. *Sterilization Of Food In Retort Pouches*, 2006, p. 33-44.

[31] https://www.simscale.com/docs/simwiki/numerics-background/what-are-the-navier-stokes-equations/#:~:text=What%20Are%20the%20Navier%2DStokes,is%20driven%20by%20various%20properties.

[32] MARION, Martine; TEMAM, Roger. Navier-Stokes equations: Theory and approximation. *Handbook of numerical analysis*, 1998, vol. 6, p. 503-689.

[33] GIRAULT, Vivette; RAVIART, Pierre-Arnaud. *Finite element methods for Navier-Stokes equations: theory and algorithms*. Springer Science & Business Media, 2012.

[34] LI, Jian; LIN, Xiaolin; CHEN, Zhangxing. *Finite Volume Methods for the Incompressible Navier-Stokes Equations*. Berlin: Springer, 2022.

[35] STRIKWERDA, John C. Finite difference methods for the Stokes and Navier–Stokes equations. *SIAM Journal on Scientific and Statistical Computing*, 1984, vol. 5, no 1, p. 56-68.

[36] D. Schlereth, Dissertation, Technical University of Munich, 2015.

[37] STRANG, Gilbert. Piecewise polynomials and the finite element method. 1973.

[38] MAURYA, Mithilesh, et al. Stabilization and Acceleration of CFD Simulation by Controlling Relaxation Factor Based on Residues: An SNN Based Approach.

[39] MARTÍNEZ, J., et al. Influence of momentum interpolation methods on the accuracy and convergence of pressure–velocity coupling algorithms in OpenFOAM®. *Journal of Computational and Applied Mathematics*, 2017, vol. 309, p. 654-673.

[40] GEORGE, Ginu R., et al. Radial heat transport in a fixed-bed reactor made of metallic foam pellets: Experiment and Particle-resolved Computational Fluid Dynamics. *International Journal of Heat and Mass Transfer*, 2022, vol. 197, p. 123376.

[41] QUADBECK, P., et al. Open cell metal foams-application-oriented structure and material selection. *Proceedings of the CELLMAT*, 2010.

[42] B. Kriszt et al., Steel Grips 1 2003, 374-379

[43] VIGNOLES, Gerard L.; ORTONA, Alberto. Numerical study of effective heat conductivities of foams by coupled conduction and radiation. *International Journal of Thermal Sciences*, 2016, vol. 109, p. 270-278.

[44] SCHUETZ, M. A.; GLICKSMAN, Leon R. A basic study of heat transfer through foam insulation. *Journal of Cellular Plastics*, 1984, vol. 20, no 2, p. 114-121.

[45] HUO, Wei, et al. Experimental study of pore diffusion effect on char gasification with CO2 and steam. *Fuel*, 2014, vol. 131, p. 59-65.

[46] GAO, Xingyuan, et al. State-of-art modifications of heterogeneous catalysts for CO2 methanation-active sites, surface basicity and oxygen defects. *Catalysis Today*, 2022.

[47] C. Panaritis, C. Michel, M. Couillard, E.A. Baranova, S.N. Steinmann, Elucidating the role of electrochemical polarization on the selectivity of the CO2 hydrogenation reaction over Ru, Electrochim. Acta 350 (2020), 136405.

[48] TAHIR, Beenish, et al. 2D/2D Mt/m-CN composite with enriched interface charge transfer for boosting photocatalytic CO2 hydrogenation by H2 to CH4 under visible light. *Applied Surface Science*, 2020, vol. 520, p. 146296.

[49] BUENO-ALEJO, Carlos J., et al. LED-driven continuous flow carbon dioxide hydrogenation on a nickel-based catalyst. *Catalysis Today*, 2020, vol. 355, p. 678-684.

[50] GÖTZ, Manuel; KOCH, Amy McDaniel; GRAF, Frank. State of the art and perspectives of CO2 methanation process concepts for power-to-gas applications. En *International Gas Union Research Conference*. Fornebu, Norway: International Gas Union, 2014.

[51] KOPYSCINSKI, Jan; SCHILDHAUER, Tilman J.; BIOLLAZ, Serge MA. Production of synthetic natural gas (SNG) from coal and dry biomass–A technology review from 1950 to 2009. *Fuel*, 2010, vol. 89, no 8, p. 1763-1783.

[52] GÓMEZ, Laura, et al. Performance study of a methanation process for a syngas obtained from a sorption enhanced gasification process. *Chemical Engineering Science*, 2023, vol. 267, p. 118291.

[53] LEFEBVRE, Jonathan; BAJOHR, Siegfried; KOLB, Thomas. A comparison of two-phase and three-phase CO2 methanation reaction kinetics. *Fuel*, 2019, vol. 239, p. 896-904.

[54] LEFEBVRE, Jonathan, et al. A study on three-phase CO2 methanation reaction kinetics in a continuous stirred-tank slurry reactor. *Fuel*, 2018, vol. 217, p. 151-159.

[55] YOUNAS, Muhammad, et al. Recent advancements, fundamental challenges, and opportunities in catalytic methanation of CO2. *Energy & Fuels*, 2016, vol. 30, no 11, p. 8815-8831.

[56] CALBRY-MUZYKA, Adelaide S.; SCHILDHAUER, Tilman J. Direct methanation of biogas—technical challenges and recent progress. *Frontiers in Energy Research*, 2020, vol. 8, p. 570887.

[57] GAO, Jiajian, et al. Recent advances in methanation catalysts for the production of synthetic natural gas. *Rsc Advances*, 2015, vol. 5, no 29, p. 22759-22776.

[58] EWALD, Stefan, et al. On the deactivation of Ni-Al catalysts in CO2 methanation. *Applied Catalysis A: General*, 2019, vol. 570, p. 376-386.

[59] ROBERTSON, S. D., et al. Determination of reducibility and identification of alloying in copper-nickel-on-silica catalysts by temperature-programmed reduction. *Journal of Catalysis*, 1975, vol. 37, no 3, p. 424-431.

[60] SEEMANN, Martin; THUNMAN, Henrik. Methane synthesis. En *Substitute natural gas from waste*. Academic Press, 2019. p. 221-243.

[61] KOPYSCINSKI, Jan; SCHILDHAUER, Tilman J.; BIOLLAZ, Serge MA. Employing catalyst fluidization to enable carbon management in the synthetic natural gas production from biomass. *Chemical Engineering & Technology: Industrial Chemistry‐Plant Equipment‐Process Engineering‐Biotechnology*, 2009, vol. 32, no 3, p. 343-347.

[62] SUDIRO, Maria; BERTUCCO, Alberto. Synthetic Natural Gas (SNG) from coal and biomass: a survey of existing process technologies, open issues and perspectives. *Natural gas*, 2010, p. 105-126.

[63] SCHAAF, Tanja, et al. Methanation of CO2-storage of renewable energy in a gas distribution system. *Energy, Sustainability and Society*, 2014, vol. 4, no 1, p. 1-14.

[64] MOZAFFARIAN, M.; ZWART, R. WR. Feasibility of SNG production by biomass hydrogasification. 2002.

[65] Zentrum fuer Sonnenenergie und Wasserstoff-Forschung. AER-gasification with in situ hot gas cleaning using biomass for poly-generation, 2006. .

[66] THEMA, Martin; BAUER, Franz; STERNER, Michael. Power-to-Gas: Electrolysis and methanation status review. *Renewable and Sustainable Energy Reviews*, 2019, vol. 112, p. 775-787.

[67] BAILERA, Manuel, et al. Power to Gas projects review: Lab, pilot and demo plants for storing renewable energy and CO2. *Renewable and Sustainable Energy Reviews*, 2017, vol. 69, p. 292-312.

[68] GHAIB, Karim; BEN-FARES, Fatima-Zahrae. Power-to-Methane: A state-of-the-art review. *Renewable and Sustainable Energy Reviews*, 2018, vol. 81, p. 433-446.

[69] WULF, Christina; LINßEN, Jochen; ZAPP, Petra. Review of power-to-gas projects in Europe. *Energy Procedia*, 2018, vol. 155, p. 367-378.

[70] LIAO, Minfang; LIU, Chengxi; QING, Zeng. A recent overview of power-to-gas projects. En *2020 IEEE 4th Conference on Energy Internet and Energy System Integration (EI2)*. IEEE, 2020. p. 2282-2286.

[71] YOUNAS, Muhammad, et al. Recent advancements, fundamental challenges, and opportunities in catalytic methanation of CO2. *Energy & Fuels*, 2016, vol. 30, no 11, p. 8815-8831.

[73] https://ars.els-cdn.com/content/image/3-s2.0-B9780081011270000064-f06-01-9780081011270.jpg

[74] NEUBERT, Michael, et al. Simulation-based evaluation of a two-stage small-scale methanation unit for decentralized applications. *Energy & Fuels*, 2017, vol. 31, no 2, p. 2076-2086.

[75] https://doc.cfd.direct/notes/cfd-general-principles/under-relaxation.

7. APPENDIX

First part:

```
#include "udf.h"
#define rho_cat 1380.0
#define hf_h2o -241.823
#define hf_h2 0.0
#define hf_co2 -393.51
#define hf_co -110.52
#define hf_ch4 -74.87

#define co2 0
#define co 1
#define h2o 2
#define h2 3
#define ch4 4
#define n2 5
#define sum 6
#define heat7 7

#define NUMLUDM 8
#define co2_source_cell(c, t) C_UDMI(c, t, 0)
#define co_source_cell(c, t) C_UDMI(c, t, 1)
#define h2o_source_cell(c, t) C_UDMI(c, t, 2)
#define h2_source_cell(c, t) C_UDMI(c, t, 3)
#define ch4_source_cell(c, t) C_UDMI(c, t, 4)
#define R1_cell(c, t) C_UDMI(c, t, 5)
#define R2_cell(c, t) C_UDMI(c, t, 6)
#define energy_source_cell(c, t) C_UDMI(c, t, 7)
```

Second part:

```
real rates(cell_t c, Thread *t, int i)
{
real mw[6] = {44.01, 28.01, 18.01528, 2.01594, 16.04, 28.0134};
real nu_1[6] = {0.0, -1.0, 1.0, -3.0, 1.0, 0.0};
real nu_2[6] = {1.0, -1.0, -1.0, 1.0, 0.0, 0.0};

real T = C_T(c,t);
real P = C_P(c,t);
real rho = C_R(c,t);
real y_ch4 = C_YI(c, t, ch4);
real y_h2 = C_YI(c, t, h2);
real y_co2 = C_YI(c, t, co2);
real y_co = C_YI(c, t, co);
real y_h2o = C_YI(c, t, h2o);
real p_ch4, p_h2, p_co2, p_co, p_h2o, k_1, K_C, K_H, K_Meth, k_2, K_CO, K_H2,
K_CH4, K_H2O, K_WGS;
```

```
real R_1_denomi, R_1a, R_1b, R_1c, R_1, R_2_denomi, R_2a, R_2, ri, R_1_1,
R_2_2;
```

Third part:

```
p_ch4 = rho*y_ch4/mw[ch4]*8314*T;
p_h2 = rho*y_h2/mw[h2]*8314*T;
p_co2 = rho*y_co2/mw[co2]*8314*T;
p_co = rho*y_co/mw[co]*8314*T;
p_h2o = rho*y_h2o/mw[h2o]*8314*T;
```

Fourth part:

```
k_1 = 1.94e7*exp(-103000/(8.314*T));
K_C = 1.83e-6*exp(42000/(8.314*T));
K_H = 5.06e-5*exp(16000/(8.314*T));
K_Meth = (1/1.027e10)*exp(26830/T-30.11);
k_2 = 2.18e-2*exp(-62000/(8.314*T));
K_CO = 8.23e-10*exp(70650/(8.314*T));
K_H2 = 6.12e-14*exp(82900/(8.314*T));
K_CH4 = 6.65e-9*exp(38200/(8.314*T));
K_H2O = 1.77e5*exp(-88680/(8.314*T));
K_WGS = exp(4400/T-4.063);
```

Fifth part:

```
R_1_denomi = (1+K_C*pow(p_co+1e-2, 0.5)+K_H*pow(p_h2+1e-2, 0.5));
R_1a = k_1*K_C*pow(K_H, 2);
R_1b = pow(p_co+1e-2, 0.5)*p_h2;
R_1c = (p_ch4+1e-2)*(p_h2o+1e-2)*pow(p_co+1e-2, -0.5)*pow(p_h2+1e-2, -2);
R_1_1 = (R_1a*(R_1b-(R_1c/K_Meth)))/pow(R_1_denomi, 3.0);
if(R_1_1<0.0005)
{
  R_1=R_1_1;
}
else
{
  R_1=0.0005;
}
R1_cell(c, t) = R_1;

R_2_denomi = (1+K_CO*(p_co+1e-2)+K_H2*(p_h2+1e-2)+K_CH4*(p_ch4+1e-
2)+K_H2O*(p_h2o+1e-2)*pow(p_h2+1e-2, -1));
R_2a = p_h2*p_co2/(K_WGS);
R_2_2 = ((k_2/(p_h2+1e-2))*(((p_co+1e-2)*(p_h2o+1e-2))-R_2a))/pow(R_2_denomi,
2.0);
if(R_2_2>-0.0005)
{
  R_2=R_2_2;
}
```

```
else
{
  R_2=-0.0005;
}
R2_cell(c, t) = R_2;}
```

Sixth part:

```
ri = (nu_1[i]*R_1+nu_2[i]*R_2)*mw[i]*rho_cat;
return ri;
}
```

Seventh part:

```
DEFINE_SOURCE(ch4_source, c, t, dS, eqn)
{
real source;
source = rates(c, t, ch4);
dS[eqn] = 0;
ch4_source_cell(c, t) = source;
return source;
}

DEFINE_SOURCE(h2_source, c, t, dS, eqn)
{
real source;
source = rates(c, t, h2);
dS[eqn] = 0;
h2_source_cell(c, t) = source;
return source;
}

DEFINE_SOURCE(co2_source, c, t, dS, eqn)
{
real source;
source = rates(c, t, co2);
dS[eqn] = 0;
co2_source_cell(c, t) = source;
return source;
}

DEFINE_SOURCE(co_source, c, t, dS, eqn)
{
real source;
source = rates(c, t, co);
dS[eqn] = 0;
co_source_cell(c, t) = source;
return source;
}
```

```
DEFINE_SOURCE(h2o_source, c, t, dS, eqn)
{
real source;
source = rates(c, t, h2o);
dS[eqn] = 0;
h2o_source_cell(c, t) = source;
return source;
}

DEFINE_SOURCE(energy_source, c, t, dS, eqn)
{
real source;
source = -((rates(c, t, h2o)/18.01528*hf_h2o+rates(c, t, co2)/44.01*hf_co2+rates(c, t,
co)/28.01*hf_co+rates(c, t, ch4)/16.04*hf_ch4)*1000000.0);
dS[eqn] = 0;
energy_source_cell(c, t) = source;
return source;
}
```